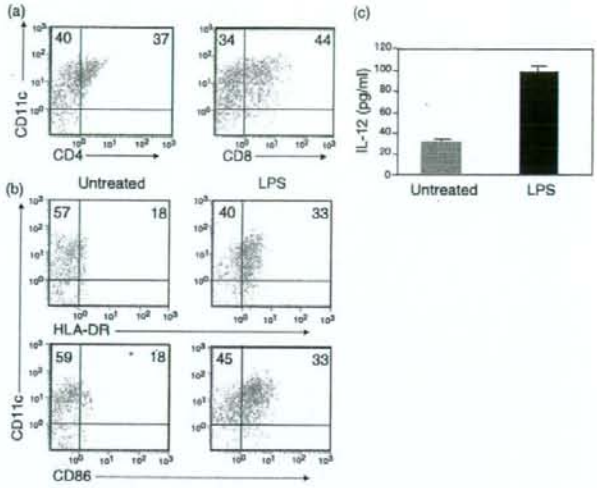

Figure 5. Characterization of splenic dendritic cells (DCs) from common marmosets (CMs). (a) Flow cytometry analysis of a low density cell fraction of splenocytes in dense bovine serum albumin (BSA). (b) The expression of human leucocyte antigen (HLA)-DR and CD86 increased in splenic CD11c$^+$ cells stimulated in culture with lipopolysaccharide (LPS; 1 μg/ml) for 24 hr. (c) Culture supernatants of splenic CD11c$^+$ cells treated with LPS for 24 hr were analysed for interleukin (IL)-12 using an enzyme-linked immunosorbent assay (ELISA).

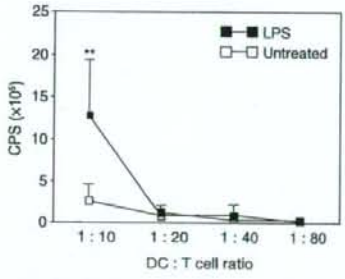

Figure 6. Xenogenic mixed leucocyte reaction (MLR) stimulatory activity of splenic dendritic cells (DCs) from common marmosets (CMs). Splenic CD11c$^+$ cells treated with or without lipopolysaccharide (LPS) stimulation (1 μg/ml) were cocultured at the indicated ratio with 6×10^4 human pan T cells for 5 days. The 5-bromo-2′ deoxyuridine (BrdU) incorporation assay showed that LPS-stimulated splenic CD11c$^+$ cells increased the proliferation of Xenogenic human T cells. The mean ± standard deviation for duplicate wells is shown. $^{**}P < 0.01$.

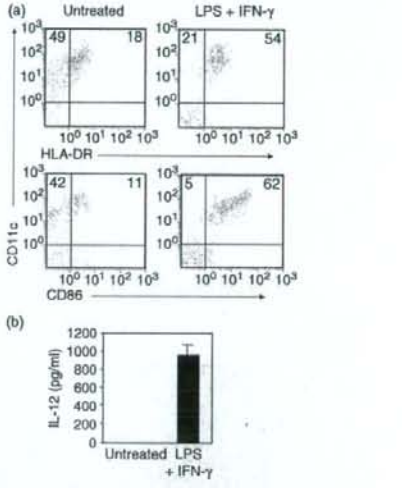

Figure 7. Characterization of monocyte-derived dendritic cells (DCs) from common marmosets (CMs). (a) Cultured CD14$^+$ cells from peripheral blood mononuclear cells (PBMC) (day 7) were stimulated with lipopolysaccharide (LPS; 1 μg/ml) and interferon (IFN)-γ (100 ng/ml) for another 24 hr. The expression of human leucocyte antigen (HLA)-DR and that of CD86 in monocyte-derived CD11c$^+$ cells were up-regulated by LPS and IFN-γ stimulation. (b) Cultured monocytes (day 7) were treated with LPS and IFN-γ for another 24 hr, and the supernatant was tested for interleukin (IL)-12 using an enzyme-linked immunosorbent assay (ELISA). Data are shown as the mean ± standard deviation. $^{**}P < 0.01$.

proliferation of xenogeneic human T cells in an MLR assay, indicating that the cells exhibited the functional features of DCs (Fig. 8).

Production of NT-3 in BM-derived DCs

We previously demonstrated that mouse splenic DCs secrete the neurotrophic factor NT-3.[7] In this study, we found that BM-derived DCs from CMs also produced NT-3 (Fig. 9). In contrast, no production of BDNF was observed from BM-derived DCs from CMs (data not shown).

Discussion

In this study, we developed methods to isolate DCs from three different CM tissues and described their phenotype

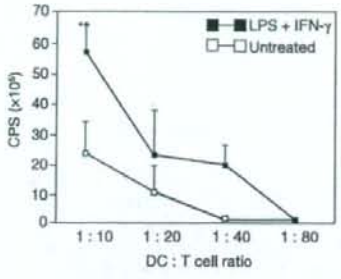

Figure 8. Monocyte-derived dendritic cells (DCs) from common marmosets (CMs) stimulated the xenogeneic mixed leucocyte reaction (MLR). Cultured monocyte-derived DCs (day 8) treated with or without lipopolysaccharide (LPS; 1 μg/ml) and interferon (IFN)-γ (100 ng/ml) for 24 hr were cocultured at the indicated ratio with 6×10^4 Xenogenic human pan T cells for 5 days. The proliferation of human T cells was then assessed by 5-bromo-2′ deoxyuridine (BrdU) incorporation. The mean ± standard deviation of duplicate wells is shown. $^{**}P < 0{\cdot}01$.

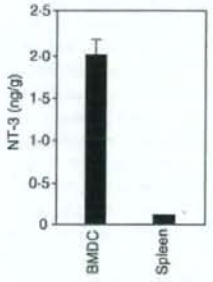

Figure 9. Bone marrow (BM)-derived dendritic cells (DCs) produced neurotrophic factor NT-3. Lysates of BM-derived DCs and spleen tissue were assayed for NT-3 using an enzyme-linked immunosorbent assay (ELISA). Data normalized by the amount of protein are shown as the mean ± standard error of the mean.

and functional capability as antigen-presenting cells. In CMs, functional analysis of DCs isolated from different tissues has previously been limited. We demonstrated that CM DCs expressed CD11c, similar to the results obtained in rhesus monkeys and humans.[43–45] Most human DCs, with the exception of plasmacytoid DCs (pDCs), express CD11c.[41] In addition, some populations of macrophages and B cells are stained with human anti-CD11c mAb.[43] Therefore, we purified $CD11c^+$ $HLA\text{-}DR^+$ cells from floating cultured BM cells to avoid contamination with fibroblasts and macrophages, which have a greater ability to attach to the dish surface than DCs. The BM-derived $CD11c^+$ cells contained populations expressing CD1a, CD1c (BDCA-1) and CD83, typical markers of human DCs,[37,38] indicating the similarity of CM DCs to human DCs. However, the expression of HLA-DR in BM-derived $CD11c^+$ cells was not high, even in mature cells. Two subsets of human DC precursors derived from cord blood $CD34^+$ cells have been identified by the exclusive expression of CD1a and CD14 at early time-points (days 5–7) in culture, and both precursor subsets mature at days 12–14 into DCs with typical morphology and phenotype: $CD1a^+$ $CD14^-$ and $CD1a^-$ $CD14^+$ precursor cells differentiate into Langerhans-type and dermal-type DCs, respectively.[46] In this study, approximately 20% of BM-derived $CD11c^+$ $HLA\text{-}DR^+$ cells expressed CD14 at day 7 in culture. Taken together, these results suggest that the BM-derived $CD11c^+$ $HLA\text{-}DR^+$ cells in the CM may contain DC precursors that exhibit relatively low expression of HLA-DR, and it may be necessary to culture them for longer times to allow them to reach maturation. It is also possible that LPS stimulation alone was not enough to allow full maturation of BM-derived DCs. Further studies are required to optimize the method for enriching immature and mature DCs derived from BM cells in the CM. Regarding the DC subtypes in CMs, we could not analyse pDCs, which may be present in peripheral blood and spleen tissue, because of a lack of available CD123 mAb in our study. To analyse the DC subtypes in the CM, more mAbs are needed that are CM-specific.

In CM, we isolated DCs from the BM, spleen and PBMC, and these DCs exhibited the functional features of antigen-presenting cells. More than 1×10^7 BM-derived DCs can be isolated from a CM specimen, and the yield from BM was 25–50 times higher than that obtained from spleen or PBMC. The yield of BM-derived DCs should be sufficient for preclinical studies on cell therapy in CM models, considering the number of DCs used for cancer immunotherapy in humans[5] or for SCI therapy in mice.[7] However, *in vivo* administration of Flt-3 ligand should be performed to determine whether this manipulation can increase the number of DCs, as reported in rhesus monkeys.[47] In view of its accessibility and lack of allograft problems, peripheral blood is a useful source of DCs; however, the amount of blood that can be isolated from a CM is limited. In this study, the maximum amount of blood obtained from a CM was 10 ml. The population of circulating human DCs in PBMC is less than 1%;[48] therefore, peripheral blood is not a good source of DCs isolated from CMs. Recently, DCs were generated from murine embryonic stem (ES) cells.[49] An ES cell line in CMs has been established;[50] thus, it may be possible to generate DCs from ES cells obtained from CMs.

Taken together, our results show that the characteristics of CM DCs resemble those of human DCs, suggesting the usefulness of CM DCs for preclinical studies on cell therapy. Moreover, we showed that BM-derived DCs from CMs also produce NT-3, an important neurotrophic factor for CNS regeneration. We are considering a preclinical study on cell therapy using BM-derived

$CD11c^+$ $HLA\text{-}DR^+$ DCs for the treatment of SCI in CMs to evaluate the therapeutic effects and safety of this procedure.

Acknowledgements

This work was supported by grants from the Ministry of Education, Science, Culture, Sports, Science and Technology (MEXT), Japan and a Grant-in-aid for the 21st Century COE programme to Keio University from MEXT. We thank Dr Reiko Ino (Beckman Coulter, Japan) for advice on the flow cytometry analysis and the gift of an antibody, and Dr Tomonori Iyoda (Kyoto University), Dr Toshiaki Ohteki (Akita University) and Dr Shigenori Nagai (Keio University) for useful discussions.

References

1 Steinman RM. The dendritic cell system and its role in immunogenicity. *Annu Rev Immunol* 1991; **9**:271–96.
2 Steinman RM, Hawiger D, Nussenzweig MC. Tolerogenic dendritic cells. *Annu Rev Immunol* 2003; **21**:685–711.
3 Nestle FO, Alijagic S, Gilliet M, Sun Y, Grabbe S, Dummer R, Burg G, Schadendorf D. Vaccination of melanoma patients with peptide- or tumor lysate-pulsed dendritic cells. *Nat Med* 1998; **4**:328–32.
4 Schuler G, Schuler-Thurner B, Steinman RM. The use of dendritic cells in cancer immunotherapy. *Curr Opin Immunol* 2003; **15**:138–47.
5 Nencioni A, Brossart P. Cellular immunotherapy with dendritic cells in cancer: current status. *Stem Cells* 2004; **22**:501–13.
6 Banchereau J, Palucka AK. Dendritic cells as therapeutic vaccines against cancer. *Nat Rev Immunol* 2005; **5**:296–306.
7 Mikami Y, Okano H, Sakaguchi M *et al.* Implantation of dendritic cells in injured adult spinal cord results in activation of endogenous neural stem/progenitor cells leading to de novo neurogenesis and functional recovery. *J Neurosci Res* 2004; **76**:453–65.
8 O'Doherty U, Ignatius R, Bhardwaj N, Pope M. Generation of monocyte-derived dendritic cells from precursors in rhesus macaque blood. *J Immunol Meth* 1997; **207**:185–94.
9 Pinchuk LM, Grouard-Vogel G, Magaletti DM, Doty RT, Andrews RG, Clark EA. Isolation and characterization of macaque dendritic cells from CD34(+) bone marrow progenitors. *Cell Immunol* 1999; **196**:34–40.
10 Pichyangkul S, Saengkrai P, Yongvanitchit K *et al.* Isolation and characterization of rhesus blood dendritic cells using flow cytometry. *J Immunol Meth* 2001; **252**:15–23.
11 Ashton-Chess J, Blancho G. An in vitro evaluation of the potential suitability of peripheral blood CD14(+) and bone marrow CD34(+)-derived dendritic cells for a tolerance inducing regimen in the primate. *J Immunol Meth* 2005; **297**:237–52.
12 Mortara L, Ploquin MJ, Faye A *et al.* Phenotype and function of myeloid dendritic cells derived from African green monkey blood monocytes. *J Immunol Meth* 2006; **308**:138–55.
13 Abbott DH, Barnett DK, Colman RJ, Yamamoto ME, Schultz-Darken NJ. Aspects of common marmoset basic biology and life history important for biomedical research. *Comp Med* 2003; **53**:339–50.
14 Ludlage E, Mansfield K. Clinical care and diseases of the common marmoset (*Callithrix jacchus*). *Comp Med* 2003; **53**:369–82.
15 Hibino H, Tani K, Sugiyama H *et al.* Haematopoietic progenitor cells from the common marmoset as targets of gene transduction by retroviral and adenoviral vectors. *Eur J Haematol* 2001; **66**:272–80.
16 t'Hart BA, Vervoordeldonk M, Heeney JL, Tak PP. Gene therapy in nonhuman primate models of human autoimmune disease. *Gene Ther* 2003; **10**:890–901.
17 Taylor-Robinson D, Furr PM, Tully JG, Barile MF, Moller BR. Animal models of *Mycoplasma genitalium* urogenital infection. *Isr J Med Sci* 1987; **23**:561–4.
18 Klug S, Neubert R, Stahlmann R, Thiel R, Ryffel B, Car BD, Neubert D. Effects of recombinant human interleukin 6 (rhIL-6) in marmosets (*Callithrix jacchus*). 1. General toxicity and hematological changes. *Arch Toxicol* 1994; **68**:619–31.
19 Genain CP, Lee-Parritz D, Nguyen MH *et al.* In healthy primates, circulating autoreactive T cells mediate autoimmune disease. *J Clin Invest* 1994; **94**:1339–45.
20 Antunes SG, de Groot NG, Brok H, Doxiadis G, Menezes AA, Otting N, Bontrop RE. The common marmoset: a new world primate species with limited Mhc class II variability. *Proc Natl Acad Sci USA* 1998; **95**:11745–50.
21 Gnanalingham KK, Smith LA, Hunter AJ, Jenner P, Marsden CD. Alterations in striatal and extrastriatal D-1 and D-2 dopamine receptors in the MPTP-treated common marmoset: an autoradiographic study. *Synapse* 1993; **14**:184–94.
22 Marshall JW, Cross AJ, Jackson DM, Green AR, Baker HF, Ridley RM. Clomethiazole protects against hemineglect in a primate model of stroke. *Brain Res Bull* 2000; **52**:21–9.
23 Kendall AL, Rayment FD, Torres EM, Baker HF, Ridley RM, Dunnett SB. Functional integration of striatal allografts in a primate model of Huntington's disease. *Nat Med* 1998; **4**:727–9.
24 Hart BA, Bauer J, Muller HJ *et al.* Histopathological characterization of magnetic resonance imaging-detectable brain white matter lesions in a primate model of multiple sclerosis: a correlative study in the experimental autoimmune encephalomyelitis model in common marmosets (*Callithrix jacchus*). *Am J Pathol* 1998; **153**:649–63.
25 t'Hart BA, Laman JD, Bauer J, Blezer E, van Kooyk Y, Hintzen RQ. Modelling of multiple sclerosis: lessons learned in a non-human primate. *Lancet Neurol* 2004; **3**:588–97.
26 Barros M, Boere V, Huston JP, Tomaz C. Measuring fear and anxiety in the marmoset (*Callithrix penicillata*) with a novel predator confrontation model: effects of diazepam. *Behav Brain Res* 2000; **108**:205–11.
27 Iwanami A, Kaneko S, Nakamura M *et al.* Transplantation of human neural stem cells for spinal cord injury in primates. *J Neurosci Res* 2005; **80**:182–90.
28 Iwanami A, Yamane J, Katoh H *et al.* Establishment of graded spinal cord injury model in a nonhuman primate: the common marmoset. *J Neurosci Res* 2005; **80**:172–81.
29 Neubert R, Foerster M, Nogueira AC, Helge H. Cross-reactivity of antihuman monoclonal antibodies with cell surface receptors in the common marmoset. *Life Sci* 1996; **58**:317–24.
30 Brok HP, Hornby RJ, Griffiths GD, Scott LA, Hart BA. An extensive monoclonal antibody panel for the phenotyping of

leukocyte subsets in the common marmoset and the cotton-top tamarin. *Cytometry* 2001; **45**:294–303.

31 Izawa K, Tani K, Nakazaki Y *et al.* Hematopoietic activity of common marmoset CD34 cells isolated by a novel monoclonal antibody MA24. *Exp Hematol* 2004; **32**:843–51.

32 Kurita R, Sasaki E, Yokoo T *et al.* Tal1/Scl gene transduction using a lentiviral vector stimulates highly efficient hematopoietic cell differentiation from common marmoset (*Callithrix jacchus*) embryonic stem cells. *Stem Cells* 2006; **24**:2014–22.

33 Lutz MB, Kukutsch N, Ogilvie AL, Rossner S, Koch F, Romani N, Schuler G. An advanced culture method for generating large quantities of highly pure dendritic cells from mouse bone marrow. *J Immunol Meth* 1999; **223**:77–92.

34 Inaba K, Inaba M, Deguchi M, Hagi K, Yasumizu R, Ikehara S, Muramatsu S, Steinman RM. Granulocytes, macrophages, and dendritic cells arise from a common major histocompatibility complex class II-negative progenitor in mouse bone marrow. *Proc Natl Acad Sci USA* 1993; **90**:3038–42.

35 Hibino H, Tani K, Ikebuchi K *et al.* The common marmoset as a target preclinical primate model for cytokine and gene therapy studies. *Blood* 1999; **93**:2839–48.

36 Schnyder B, Lugli SM, Schnyder-Candrian S, Eng VM, Moser R, Banchereau J, Ryffel B, Car BD. Biochemical and morphological characterization of vascular and lymphocytic interleukin-4 receptors. *Am J Pathol* 1996; **149**:1369–79.

37 Dzionek A, Fuchs A, Schmidt P, Cremer S, Zysk M, Miltenyi S, Buck DW, Schmitz J. BDCA-2, BDCA-3, and BDCA-4: three markers for distinct subsets of dendritic cells in human peripheral blood. *J Immunol* 2000; **165**:6037–46.

38 Cao X, Sugita M, Van Der Wel N, Lai J, Rogers RA, Peters PJ, Brenner MB. CD1 molecules efficiently present antigen in immature dendritic cells and traffic independently of MHC class II during dendritic cell maturation. *J Immunol* 2002; **169**:4770–7.

39 Ohteki T, Fukao T, Suzue K, Maki C, Ito M, Nakamura M, Koyasu S. Interleukin 12-dependent interferon gamma production by CD8alpha+ lymphoid dendritic cells. *J Exp Med* 1999; **189**:1981–6.

40 Inaba K, Swiggard WJ, Steinman RM, Romani N, Schuler G, eds. *Isolation of Dendritic Cells.* Hoboken, NJ: John Wiley & Sons, Inc., 2003.

41 Shortman K, Liu YJ. Mouse and human dendritic cell subtypes. *Nat Rev Immunol* 2002; **2**:151–61.

42 Kamath AT, Pooley J, O'Keeffe MA *et al.* The development, maturation, and turnover rate of mouse spleen dendritic cell populations. *J Immunol* 2000; **165**:6762–70.

43 McIlroy D, Troadec C, Grassi F *et al.* Investigation of human spleen dendritic cell phenotype and distribution reveals evidence of in vivo activation in a subset of organ donors. *Blood* 2001; **97**:3470–7.

44 Ito T, Inaba M, Inaba K *et al.* A CD1a+/CD11c+ subset of human blood dendritic cells is a direct precursor of Langerhans cells. *J Immunol* 1999; **163**:1409–19.

45 Teleshova N, Kenney J, Jones J *et al.* CpG-C immunostimulatory oligodeoxyribonucleotide activation of plasmacytoid dendritic cells in rhesus macaques to augment the activation of IFN-gamma-secreting simian immunodeficiency virus-specific T cells. *J Immunol* 2004; **173**:1647–57.

46 Caux C, Vanbervliet B, Massacrier C *et al.* CD34+ hematopoietic progenitors from human cord blood differentiate along two independent dendritic cell pathways in response to GM-CSF+TNF alpha. *J Exp Med* 1996; **184**:695–706.

47 Coates PT, Barratt-Boyes SM, Zhang L *et al.* Dendritic cell subsets in blood and lymphoid tissue of rhesus monkeys and their mobilization with Flt3 ligand. *Blood* 2003; **102**:2513–21.

48 Fearnley DB, Whyte LF, Carnoutsos SA, Cook AH, Hart DN. Monitoring human blood dendritic cell numbers in normal individuals and in stem cell transplantation. *Blood* 1999; **93**:728–36.

49 Senju S, Hirata S, Matsuyoshi H, Masuda M, Uemura Y, Araki K, Yamamura K, Nishimura Y. Generation and genetic modification of dendritic cells derived from mouse embryonic stem cells. *Blood* 2003; **101**:3501–8.

50 Sasaki E, Hanazawa K, Kurita R *et al.* Establishment of novel embryonic stem cell lines derived from the common marmoset (*Callithrix jacchus*). *Stem Cells* 2005; **23**:1304–13.

The International Journal of Biochemistry & Cell Biology 40 (2008) 1649–1653

Contents lists available at ScienceDirect

The International Journal of Biochemistry & Cell Biology

journal homepage: www.elsevier.com/locate/biocel

Medicine in focus

Spinal cord injury: Emerging beneficial role of reactive astrocytes' migration

Francois Renault-Mihara[a,b], Seiji Okada[a,c], Shinsuke Shibata[a], Masaya Nakamura[b], Yoshiaki Toyama[b], Hideyuki Okano[a,*]

[a] Department of Physiology, Keio University School of Medicine, 35 Shinanomachi, Shinjuku-ku, Tokyo 160-8582, Japan
[b] Department of Orthopedic Surgery, Keio University School of Medicine, 35 Shinanomachi, Shinjuku-ku, Tokyo 160-8582, Japan
[c] SSP Stem Cell Unit, Graduate School of Medical Science, Kyushu University, 3-1-1 Maidashi, Higashi-ku, Fukuoka 812-8582, Japan

ARTICLE INFO

Article history:
Received 3 January 2008
Received in revised form 3 March 2008
Accepted 10 March 2008
Available online 16 March 2008

Keywords:
Spinal cord injury
Reactive astrocyte
Migration
Therapeutic

ABSTRACT

Spinal cord injury (SCI), despite considerable progress in palliative care, has currently no satisfying therapeutic leading to functional recovery. Inability of central nervous system severed axons to regenerate after injury is considered to originate from both limited intrinsic capabilities of neurons and inhibitory effect of the local environment. Precisely, the so-called "glial scar" formed by reactive astrocytes in response to injury exerts a well-known axon-outgrowth inhibitory effect. However, recent studies revealed that role of reactive astrocytes after SCI is more complex. During the first weeks after injury, reactive astrocytes indeed protect the tissue and contribute to a spontaneous relative functional recovery. Compaction of the lesion center and seclusion of inflammatory cells by migrating reactive astrocytes seem to underlie this beneficial effect. Stimulation of reactive astrocytes migration in the sub-acute phase of SCI might thus represent a new approach to improve the functional outcome of patients.

1. Introduction

Spinal cord injury (SCI) is a life threatening condition without complete cure. The incidence rate of SCI ranges from 13.1 to 27.1 cases per million per year (Jackson et al., 2004), with the most common etiology for traumatic SCI being car accident (43–50%) followed by falls (18.8–37%) and violence (17.8%), specially gunshot wounds in United States. Clinically, SCI leads to a complete loss of motor, sensory and vegetative functions underneath the point of injury. Since a high proportion of the SCI occurs at the cervical spine about 40% of the patients suffer from quadriplegia (Schwab et al., 2006). It is noteworthy that the survival rate of patients with acute traumatic SCI has dramatically increased these last decades (from 5% at the beginning of the second world war, to 95% nowadays (Schwab et al., 2006)), thanks to the development of therapies allowing extensive anatomical reconstruction of bone structure (including specially modern methods for osteosynthesis). Although the majority of patients with SCI are able to return to a relatively independent life, they retain a life-long handicap. Since the patients sustaining traumatic SCI are predominantly young, with a mean age of 32 years (Jackson et al., 2004), the real socio-economical impact of SCI is much more important than the costs for medical and surgical care.

2. Pathogenesis of SCI

SCI consists of a two-steps process involving a primary mechanical injury followed by an inflammatory process characterized by infiltration of inflammatory cells

* Corresponding author at: Department of Physiology, Keio University School of Medicine, 35 Shinanomachi, Shinjuku-ku, Tokyo 160-8582, Japan. Tel.: +81 3 5363 3747; fax: +81 3 3357 5445.
E-mail address: hidokano@sc.itc.keio.ac.jp (H. Okano).

1357-2725/$ – see front matter © 2008 Elsevier Ltd. All rights reserved.
doi:10.1016/j.biocel.2008.03.009

in the lesion center and appearance of reactive astrocytes.

The primary damage is locally restricted to the area of the vertebral fracture and is characterized by acute hemorrhage and ischemia. Secondary insult within the first week after injury is characterized by further destruction of neuronal and glial cells, and leads to important expansion of the damage, so that the paralysis can extend to higher segments. This review will focus specifically on emerging roles of reactive astrocytes on the second step (inflammatory process) after SCI. For an extensive view of the glial inhibition of CNS axon regeneration please refer to recent reviews (Silver and Miller, 2004; Yiu and He, 2006).

At the cellular level, Ramòn y Cajal (1928) described more than one century ago that the ends of proximal injured axons become swollen into "dystrophic endballs" (called now retraction-bulbs). It is now clear that distal axon ends also degrade, through a Wallerian degeneration process. Moreover, in the center of the injury appears a pseudo-cyst, a fluid-filled cavity, which is then surrounded by the glial scar that is composed of different types of cells (astrocytes, microglia and fibroblasts) as well as secreted extracellular molecules. SCI pathology results from complex interactions between all these different cell types and secreted molecules in a time-dependent context.

3. Reactive astrocytes: formerly known as bad guys

Ramòn y Cajal (1928) believed that the injured neurons of the CNS were no longer capable of regeneration. Whereas this inability to regenerate might be partly attributed to the gradual decline in the intrinsic growth ability of neurons associated with aging, the fact that injured axons can extend over long distance in the permissive environment of a peripheral nerve graft (David and Aguayo, 1981) demonstrated a major inhibitory effect of the local environment. Noteworthy, dorsal root ganglia neurons have axons in both the CNS and PNS, but can only regenerate their peripheral processes. This extrinsic inhibition seems to be related in part to myelin inhibitors (Yiu and He, 2006), that are exposed to severed axons after damage of the structure of the myelin, which normally ensheaths nerve fibers. Another major source of inhibition originates from the glial scar, which is considered as a physical and molecular barrier to regeneration. Formation of the glial scar occurs after the introduction of non-CNS molecules into the brain parenchyma as a result of the blood–spinal cord barrier disruption which is initiated by both mechanical forces and inflammatory mediators. Blood–spinal cord barrier remains indeed porous to blood and serum components for up to 2 weeks after SCI, and areas of greatest glial scarring correlate with areas of most extensive blood–spinal cord barrier breakdown, as well as the largest numbers of activated macrophages. Noteworthy complete formation of the glial scar does require several weeks, and can persist for several months after SCI (Silver and Miller, 2004). In lesions that spare the dura mater, the scar is composed primarily of reactive astrocytes, but in more severe lesions that open the meninges, astroglia become mixed with invading connective tissue elements.

The astrocyte response to injury is referred to as reactive astrogliosis (literally, *more glia*), but in fact the amount of glial cell division is relatively limited, and confined to the immediate penumbra surrounding the lesion center. Astrocyte reactivity is characterized by a cellular hypertrophy with processes extension and increased production of intermediate filaments, such as, e.g. glial fibrillary acidic protein (GFAP) and vimentin. Since glial scars formed after injury are less dense in double GFAP$^{-/-}$ vimentin$^{-/-}$ mice, these proteins seem to be required for proper glial scar formation (Pekny et al., 1999). Unaffected formation of glial scar and sub-normal phenotype after SCI in single knockout mice for GFAP or vimentin however indicates that some degree of functional overlap does exist between these intermediate filaments proteins (Pekny et al., 1999; Wang et al., 1997).

Reactive astrocytes also secrete proteoglycans, extracellular matrix molecules that consists of a protein core linked by four sugar moieties to a sulphated glycosaminoglycan chain. One of the four classes of proteoglycans, the chondroitin sulphate proteoglycan (CSPG), has been demonstrated in a large number of studies to inhibit both in vitro and in vivo axonal regeneration (Schwab et al., 2006; Silver and Miller, 2004; Yiu and He, 2006). Deglycosylation of CSPG by an enzyme, the chondroitinase ABC suppresses its inhibitory effect towards axon-growth. Local administration of chondroitinase ABC (Ikegami et al., 2005), or selective ectopic expression by astrocytes in transgenic mice (Cafferty et al., 2007) indeed increased axonal regeneration and improved functional recovery after SCI.

In addition, reactive astrocytes also produce other molecules that are known to hinder axonal outgrowth (e.g. slit proteins (Hagino et al., 2003), ephrin-B2 (Bundesen et al., 2003). The view that reactive astrocytes exert a detrimental effect after SCI has thus strong support.

4. Emerging positive role of reactive astrocytes: finally, not that wicked

Nevertheless, the basic phenomena of reactive astrocytosis after CNS injury appears to be conserved throughout evolution of vertebrates (Larner et al., 1995), suggesting that fundamental aspects of the process of reactive astrocytosis convey survival advantage. Astrocytes indeed clear glutamate and potassium ions from the extracellular space (Hertz and Zielke, 2004), are a potential energy source for neurons, and produce numerous growth factors and cytokines.

The observation that after SCI the reduced glial scars in double GFAP$^{-/-}$ vimentin$^{-/-}$ mice were frequently accompanied by bleeding indeed revealed a positive aspect of astrocyte reactivity (Pekny et al., 1999).

Faulkner et al. (2004) have recently confirmed such an idea. Mice expressing a GFAP-herpes simplex virus-thymidine kinase transgene were given mild or moderate SCI and treated with antiviral agent ganciclovir to ablate selectively and conditionally dividing, reactive, transgene-expressing astrocytes located in the lesion site. In two different injury models, ablation of dividing reactive astrocytes led to a deteriorated syndrome characterized by increased alteration of neurons and oligodendrocytes, more

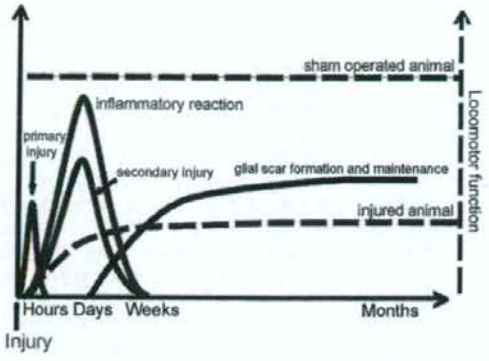

Fig. 1. Scheme recapitulating the sequential pathological events after spinal cord injury.

severe demyelination, and pronounced motor deficits. Since inflammatory reaction and secondary insult are considered to be closely linked (Fig. 1), the observation that loss of dividing reactive astrocytes after SCI led to a markedly increased and prolonged infiltration of inflammatory cells, in particular macrophages, suggests that astrocytosis controls the magnitude and/or spatial restriction of inflammatory reaction. Nevertheless, given that contribution of mitosis to the phenomenon of astrocytosis is weak, these observations that rely on ablation of the dividing pool of reactive astrocytes obviously do not reflect the whole contribution of reactive astrocytes.

Thereafter, observation by our group (Okada et al., 2006) that in the sub-acute phase after SCI (i.e. during the first 2 weeks) reactive astrocytes compact the lesion center and seem to seclude inflammatory cells (Fig. 2A) led to investigate the mediator of this astrocytic response. Signal transducer and activator of transcription 3 (STAT3), a signaling molecule involved in many biological processes,

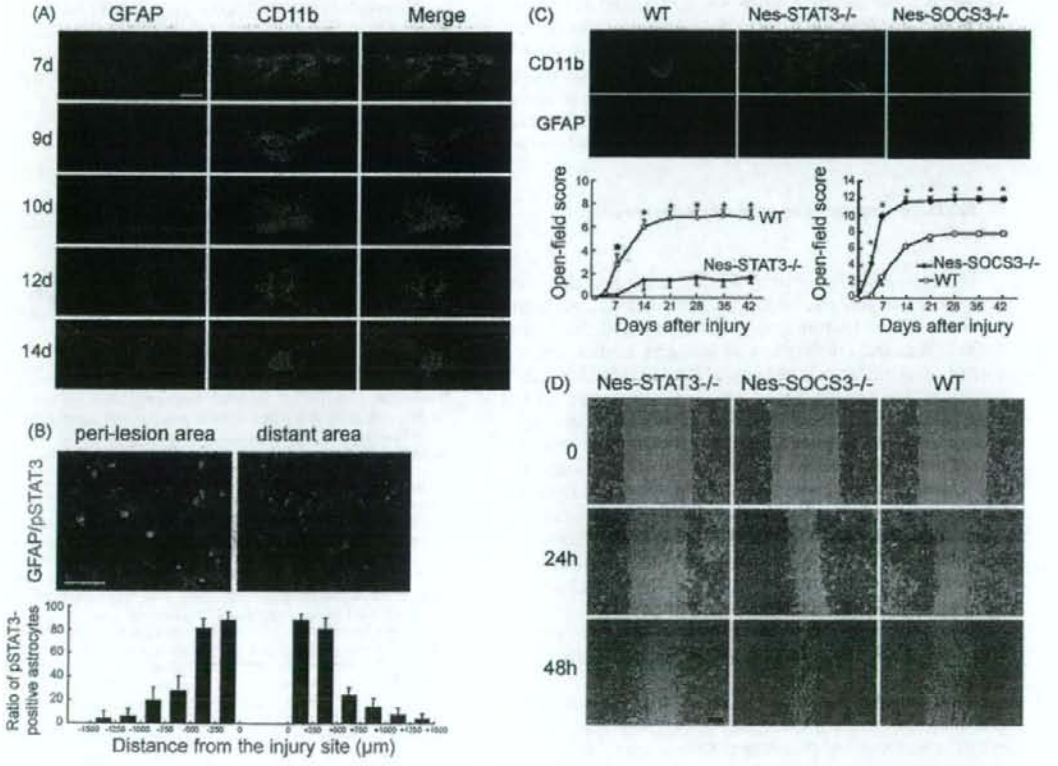

Fig. 2. Compaction of the lesion center by reactive astrocytes is correlated with enhanced functional recovery after spinal cord injury. (A) During the first 2 weeks after SCI, reactive astrocytes (immunolabelled by GFAP) compact the lesion center and seclude inflammatory cells (CD11b). (B) Colocalization between phospho-STAT3 and GFAP demonstrates that STAT3 is activated in reactive astrocytes surrounding the lesion site. (C) Compaction of the lesion center by reactive astrocytes depends on STAT3 signaling and is correlated with enhanced functional recovery after SCI. Upper panels show strongly impaired compaction of lesion center in Nes-STAT3$^{-/-}$ mice, compared to wild-type mice at 14 days after injury, whereas stimulation of STAT3 in Nes-SOCS3$^{-/-}$ mice led to improved compaction. Bottom graphs show that functional recovery after SCI relies on STAT3 signaling in reactive astrocytes. (D) Modulation of in vitro migration capabilities of astrocytes by STAT3 signaling strongly suggests that compaction of the lesion center observed in (A) is driven by astrocyte migration. Figure adapted from Okada et al. (2006).

is markedly activated in reactive astrocytes surrounding the injury site (Fig. 2B), thus questioning the role of STAT3 in reactive astrocytes after SCI. Since nestin, an intermediate filament, is re-expressed in reactive astrocytes, use of the Cre-LoxP system, by mating Nestin-Cre mice with $STAT3^{loxP/loxP}$ mice, allowed selective and conditional ablation of STAT3 in reactive astrocytes after SCI. Strikingly, the conditional knock-out mice targeting STAT3 (Nes-$STAT3^{-/-}$) displayed severe impairment of lesion center compaction (Fig. 2C, upper panel). Conversely, selective enhancement of STAT3 signaling by ablation of SOCS3, a negative regulator of STAT3, led to increased compaction of the lesion center. Moreover, whereas the functional recovery that occurs spontaneously in wild-type animals was reduced in Nes-$STAT3^{-/-}$ mice, Nes-$SOCS3^{-/-}$ mice accordingly displayed an improved locomotor recovery (Fig. 2C, bottom panel). These results indicate that compaction of the lesion center by reactive astrocytes depends on STAT3 signaling and is correlated with enhanced functional recovery. Since BrdU incorporation experiments did not reveal any difference in term of proliferation between these different mice, we speculated that compaction of the lesion would be driven by migration of the reactive astrocytes. Accordingly, in vitro wound scratch assay revealed that STAT3 positively regulates astrocyte migration (Fig. 2D). This suggests that migration of astrocytes, by compacting the lesion center and secluding inflammatory cells, contributes to functional recovery after SCI.

5. Reactive astrocytes as potential therapeutic targets

The recent studies related above clearly revealed that reactive astrocytes should not be seen only as detrimental after SCI. In two of these studies, even if the injury differs (stab and crush injury in study by Faulkner et al., contusion in our work), the beneficial role of reactive astrocytes was revealed during the sub-acute phase after SCI, i.e. before glial scar forms. The long lasting glial scar (up to several months after SCI) seems to underlie the detrimental effect of reactive astrocytes in the chronic phase after SCI. Proof of concept of the inhibition of the axon-outgrowth inhibitory properties of the glial scar during the chronic phase has indeed already been established (Cafferty et al., 2007; Ikegami et al., 2005). Since it is difficult to cover all of the issues related to reactive astrocytes and SCI within a limited space, please refer to recent reviews (Pekny et al., 2007; Sofroniew, 2005) for an extensive view on neuropathology and inhibitory actions of reactive astrocytes at later stages.

Targeting reactive astrocytes during the sub-acute phase after SCI might also have some therapeutic interest. It is noteworthy that Nes-$SOCS3^{-/-}$ mice display an enhanced recovery after SCI. Thus cell specific modulation of STAT3-mediated mechanism in the sub-acute phase should enhance the therapeutic effects. However, therapeutic potentials remain at present highly speculative and need to be substantiated by further studies. Especially, the molecular effectors whereby STAT3 governs intrinsic astrocyte migration remain to be determined. In our study (Okada et al., 2006) we observed that upon ablation of STAT3, repression of E-cadherin expression, through LIV1, was lost, which may originate increased adhesion of Nes-$STAT3^{-/-}$ astrocytes and thereby reduced migration capabilities. Since E-cadherin is not expressed in wild-type astrocytes, this mechanism does nevertheless not explain the increased migration of Nes-$SOCS3^{-/-}$ astrocytes. Ongoing research aims at identifying the mediators whereby STAT3 controls positively astrocyte migration. Another important point, with regards the possibility to modulate migration of astrocytes after SCI concerns the nature and origin of the signals that initiate and orientate this migration. Since blood–spinal cord barrier remains porous to blood and serum components for up to 14 days after SCI, i.e. during the maximum compaction of lesion center, astrocytes might be attracted by soluble molecules derived from circulating flow. Another hypothesis is that due to hemorrhage, local entry of blood elements, such as platelets or activated macrophages contributes to create a chemotactic gradient.

Although currently highly speculative, future elucidation of both intrinsic and extrinsic astrocyte migration's mechanisms, and identification of specific molecular targets might thus contribute to ameliorate the functional outcome of patients.

References

Bundesen LQ, Scheel TA, Bregman BS, Kromer LF. Ephrin-B2 and EphB2 regulation of astrocyte–meningeal fibroblast interactions in response to spinal cord lesions in adult rats. J Neurosci 2003;23(21):7789–800.

Cafferty WB, Yang SH, Duffy PJ, Li S, Strittmatter SM. Functional axonal regeneration through astrocytic scar genetically modified to digest chondroitin sulfate proteoglycans. J Neurosci 2007;27(9):2176–85.

David S, Aguayo AJ. Axonal elongation into peripheral nervous system "bridges" after central nervous system injury in adult rats. Science 1981;214(4523):931–3.

Faulkner JR, Herrmann JE, Woo MJ, Tansey KE, Doan NB, Sofroniew MV. Reactive astrocytes protect tissue and preserve function after spinal cord injury. J Neurosci 2004;24(9):2143–55.

Hagino S, Iseki K, Mori T, Zhang Y, Hikake T, Yokoya S, et al. Slit and glypican-1 mRNAs are coexpressed in the reactive astrocytes of the injured adult brain. Glia 2003;42(2):130–8.

Hertz L, Zielke HR. Astrocytic control of glutamatergic activity: astrocytes as stars of the show. Trends Neurosci 2004;27(12):735–43.

Ikegami T, Nakamura M, Yamane J, Katoh H, Okada S, Iwanami A, et al. Chondroitinase ABC combined with neural stem/progenitor cell transplantation enhances graft cell migration and outgrowth of growth-associated protein-43-positive fibers after rat spinal cord injury. Eur J Neurosci 2005;22(12):3036–46.

Jackson AB, Dijkers M, Devivo MJ, Poczatek RB. A demographic profile of new traumatic spinal cord injuries: change and stability over 30 years. Arch Phys Med Rehabil 2004;85(11):1740–8.

Larner AJ, Johnson AR, Keynes RJ. Regeneration in the vertebrate central nervous system: phylogeny, ontogeny, and mechanisms. Biol Rev Camb Philos Soc 1995;70(4):597–619.

Okada S, Nakamura M, Katoh H, Miyao T, Shimazaki T, Ishii K, et al. Conditional ablation of Stat3 or Socs3 discloses a dual role for reactive astrocytes after spinal cord injury. Nat Med 2006;12(7):829–34.

Pekny M, Johansson CB, Eliasson C, Stakeberg J, Wallen A, Perlmann T, et al. Abnormal reaction to central nervous system injury in mice lacking glial fibrillary acidic protein and vimentin. J Cell Biol 1999;145(3):503–14.

Pekny M, Wilhelmsson U, Bogestal YR, Pekna M. The role of astrocytes and complement system in neural plasticity. Int Rev Neurobiol 2007;82:95–111.

Ramôn y Cajal S.May RM, editor. Degeneration and regeneration of the nervous system. London: Oxford University Press; 1928.
Schwab JM, Brechtel K, Mueller CA, Failli V, Kaps HP, Tuli SK, et al. Experimental strategies to promote spinal cord regeneration—an integrative perspective. Prog Neurobiol 2006;78(2):91–116.
Silver J, Miller JH. Regeneration beyond the glial scar. Nat Rev Neurosci 2004;5(2):146–56.
Sofroniew MV. Reactive astrocytes in neural repair and protection. Neuroscientist 2005;11(5):400–7.
Wang X, Messing A, David S. Axonal and nonneuronal cell responses to spinal cord injury in mice lacking glial fibrillary acidic protein. Exp Neurol 1997;148(2):568–76.
Yiu G, He Z. Glial inhibition of CNS axon regeneration. Nat Rev Neurosci 2006;7(8):617–27.

NeuroImage 44 (2009) 884–892

Contents lists available at ScienceDirect

NeuroImage

journal homepage: www.elsevier.com/locate/ynimg

Visualization of peripheral nerve degeneration and regeneration: Monitoring with diffusion tensor tractography☆

Takehiko Takagi [a,b], Masaya Nakamura [a], Masayuki Yamada [e,f], Keigo Hikishima [d,e], Suketaka Momoshima [c], Kanehiro Fujiyoshi [a,b], Shinsuke Shibata [b], Hirotaka James Okano [b], Yoshiaki Toyama [a], Hideyuki Okano [b,*]

[a] Department of Orthopaedic Surgery, Keio University School of Medicine, 35 Shinanomachi, Shinjuku-ku, Tokyo 160-8582, Japan
[b] Department of Physiology, Keio University School of Medicine, 35 Shinanomachi, Shinjuku-ku, Tokyo 160-8582, Japan
[c] Department of Diagnostic Radiology, Keio University School of Medicine, 35 Shinanomachi, Shinjuku-ku, Tokyo 160-8582, Japan
[d] Center for Integrated Medical Research, Keio University, 35 Shinanomachi, Shinjuku-ku, Tokyo 160-8582, Japan
[e] Central Institute for Experimental Animals, 1430 Nogawa, Miyamae-ku, Kawasaki, Kanagawa, 216-0001, Japan
[f] Faculty of Radiological Technology, Fujita Health University School of Health Sciences, 1-98 Dengakugakubo, Kutsukake-cho, Toyoake-shi, Aichi 470-1192, Japan

ARTICLE INFO

Article history:
Received 1 July 2008
Revised 15 September 2008
Accepted 17 September 2008
Available online 2 October 2008

Keywords:
Diffusion tensor imaging
Diffusion tensor tractography
Peripheral nerve injury
Fractional anisotropy
Wallerian degeneration
Magnetic resonance imaging

ABSTRACT

We applied diffusion tensor tractography (DTT), a recently developed MRI technique that reveals the microstructures of tissues based on its ability to monitor the random movements of water molecules, to the visualization of peripheral nerves after injury. The rat sciatic nerve was subjected to contusive injury, and the data obtained from diffusion tensor imaging (DTI) were used to determine the tracks of nerve fibers (DTT). The DTT images obtained using the fractional anisotropy (FA) threshold value of 0.4 clearly revealed the recovery process of the contused nerves. Immediately after the injury, fiber tracking from the designated proximal site could not be continued beyond the lesion epicenter, but the intensity improved thereafter, returning to its pre-injury level by 3 weeks later. We compared the FA value, a parameter computed from the DTT data, with the results of histological and functional examinations of the injured nerves, during recovery. The FA values of the peripheral nerves were more strongly correlated with axon-related (axon density and diameter) than with myelin-related (myelin density and thickness) parameters, supporting the theories that axonal membranes play a major role in anisotropic water diffusion and that myelination can modulate the degree of anisotropy. Moreover, restoration of the FA value at the lesion epicenter was strongly correlated with parameters of motor and sensory functional recovery. These correlations of the FA values with both the histological and functional changes demonstrate the potential usefulness of DTT for evaluating clinical events associated with Wallerian degeneration and the regeneration of peripheral nerves.

Introduction

MRI, an indispensable tool in the diagnosis of central nervous system disorders, has rarely been applied to diseases of the peripheral nervous system, because it is difficult to delineate peripheral nerves on account of their poor contrast with the surrounding tissues. The standard repertoire for diagnosing peripheral nerve disorders includes clinical and electrophysiological examinations, supplemented by more invasive procedures.

For the differential diagnosis of peripheral nerve lesions, the visualization of peripheral nerves using MRI has been attempted using special techniques such as MR neurography (Filler et al., 2004; Howe et al., 1992). However, the interpretation of the images obtained by MR neurography is based on visual inspection, and is therefore qualitative and subjective. Furthermore, since MR neurography cannot image continuous nerve fibers over their entire length, it is not considered useful for examining the growth of regenerating peripheral nerves. To visualize nerve fibers in MRI, a contrast agent such as superparamagnetic iron oxide (SPIO) (Bendszus and Stoll, 2003) or gadofluorine M (Bendszus et al., 2005; Wessig et al., 2008) can be injected, but this is invasive. The difficulty in visualizing axons makes these methods impractical for evaluating peripheral nerve injury in the present clinical scenario.

To overcome these shortcomings, here we applied diffusion tensor imaging (DTI), a non-invasive method that reveals the microstructure of tissues on the basis of its ability to monitor the random movements of water molecules (Basser et al., 1994). Diffusion tensor tractography (DTT) refers to the analysis and reconstruction of the data obtained by DTI, by which the orientation of nerve fibers can be followed to trace specific neural pathways, such as that of the corticospinal tract in the brain or the spinal cord (Conturo et al., 1999; Fujiyoshi et al., 2007; Mori and Zhang, 2006; Tuch et al., 2001). Mac Donald et al have

☆ Diffusion tensor peripheral nerve tractography.

* Corresponding author. Fax: +81 3 3357 5445.
E-mail address: hidokano@sc.itc.keio.ac.jp (H. Okano).

1053-8119/$ – see front matter © 2008 Elsevier Inc. All rights reserved.
doi:10.1016/j.neuroimage.2008.09.022

obtained results indicating that DTI may be more sensitive than conventional MRI for evaluating traumatic brain injury (Mac Donald et al., 2007b).

Recent advances in MRI technology have made it possible to delineate peripheral nerve tracts in humans (Hiltunen et al., 2005; Meek et al., 2006; Skorpil et al., 2004). However, the reliability of DTT imaging has not yet been validated with detailed histological studies and quantitative analyses, so it has remained unclear whether the changes in DTT parameters actually correspond to the anatomical degeneration and regeneration of axonal fibers. Although the disintegration of axonal structures and demyelination occurring after peripheral nerve injury, known as Wallerian degeneration, is known to reduce the anisotropy of peripheral nerves (Beaulieu et al., 1996; Stanisz et al., 2001), and DTI has been shown to be useful for detecting axonal injury after traumatic brain injury (Mac Donald et al., 2007a,b) and ischemic injury of the optic nerve (Song et al., 2003; Sun et al., 2008), peripheral nerve tracking during the process of Wallerian degeneration has never been reported. We believe that since no proper tools are presently available for the visualization of peripheral nerves, it is important to evaluate the validity of applying DTT to assess peripheral nerve degeneration and regeneration. The objectives of the present study were to determine whether DTT is useful for tracking peripheral nerves, and to determine the relevance of the tracking parameters for evaluating fibers after peripheral nerve injury, by comparing them with histological and functional parameters of recovery.

Materials and methods

Animals and surgical procedures

One hundred twenty adult female Sprague-Dawley rats (165–228 g, 7 or 8 weeks of age; Clea Japan Inc., Tokyo, Japan) were used. All interventions and animal care procedures were performed in accordance with the Laboratory Animal Welfare Act, the Guide for the Care and Use of Laboratory Animals (National Institutes of Health), and the Guidelines and Policies for Animal Surgery provided by the Animal Study Committee of Keio University, and were approved by the Ethics Committee of Keio University. All surgeries were performed under chloral hydrate anesthesia (intraperitoneal injection; 350 mg per kg body weight; Wako Pure Chemicals, Osaka, Japan). The animals were housed in groups under a 12-hour light/dark cycle, with access to food and water *ad libitum*. The sciatic nerve was exposed through a dorsal gluteal muscle-splitting approach. The nerve was then subjected to a contusive injury at the sciatic notch using a brain aneurysm clip (Sugita clip; Mizuho Ikakogyo, Tokyo, Japan). The clip was closed and left in place for 5 min with a holding force of approximately 150 g (Kato et al., 2005).

Magnetic resonance imaging

MRI was performed using a 7.0-Tesla magnet (PharmaScan 70/16; Bruker BioSpin, Ettlingen, Germany) with a 38-mm volume coil dedicated for examinations of small animals. In studies using excised sciatic nerve, intact (pre-injured) excised nerves and nerves that had been excised 3 h, 1 day, 4 days, and 1, 2, 3, 4, 6, 8, and 12 weeks after the crush injury ($n=10$ each) were embedded in 2% agarose gel with 5 mM copper sulfate, and immediately subjected to diffusion tensor MRI. DTI data sets were acquired with a spin-echo sequence based on the Stejskal-Tanner diffusion preparation (Stejskal and Tanner, 1965). The scanning parameters were as follows: repetition time (TR), 15,000 ms; echo time (TE), 40 ms; flip angle, 90°; field of view (FOV), 40×40 mm; acquisition data matrix, 128×128; reconstructed image resolution, 0.31 mm; slice thickness, 0.94 mm; number of excitations (NEX), 1; b-value, 1000 s/mm^2; and motion probing gradient (MPG) orientations, 12 axes. Table 1 shows our normalized diffusion gradient orientations; duration of diffusion gradient pulses, 7 ms; diffusion time, 14 ms. The total imaging time was 6 h, 56 min.

Table 1
Normalized diffusion gradient orientations

Image volume	Gradients		
	x	*y*	*z*
1	0.0000	0.0000	0.0000
2	0.8944	0.0000	0.4472
3	0.0000	0.4472	0.8944
4	0.4472	0.8944	0.0000
5	0.8944	0.4472	0.0000
6	0.0000	0.8944	0.4472
7	0.4472	0.0000	0.8944
8	0.8944	0.0000	−0.4472
9	0.0000	−0.4472	0.8944
10	−0.4472	0.8944	0.0000
11	0.8944	−0.4472	0.0000
12	0.0000	0.8944	−0.4472
13	−0.4472	0.0000	0.8944

Diffusion tensor analysis

Diffusion tensor tractographic images were computed using the Volume One and dTV II SR software (Masutani et al., 2003). The diffusion tensor can be represented as an ellipsoid, where a proton at the center of the voxel has an equal probability of diffusing to any point in that ellipsoid. The eigenvectors of the diffusion tensor represent the three axes of the ellipsoid, namely, the length of the longest, middle, and shortest axes (called eigenvalues λ_1, λ_2 and λ_3). The eigenvector (e_1) associated with the largest eigenvalue (λ_1) was assumed to represent the local fiber direction. Fiber tracking was initiated from a manually selected region of interest (ROI), from which tracking lines were propagated bidirectionally according to the principal eigenvector (e_1) in each voxel. For the tractography, the ROI was placed at a site 5 mm proximal to the lesion epicenter, and the direction of the diffusion anisotropy was followed until the tracking was terminated at a voxel, depending on the threshold selected, with a fractional anisotropy (FA) of less than 0.25, 0.3, 0.4, 0.5, 0.6, 0.7, or 0.75. The FA value, a convenient index because it is scaled from 0 (isotropic) to 1 (anisotropic) (Mori and Zhang, 2006), can be calculated from the degree of diffusion anisotropy (Pierpaoli and Basser, 1996).

We determined the FA values and three eigenvalues (λ_1, λ_2, and λ_3) in each specimen at points 5 mm (proximal site), 0 mm (lesion epicenter), and −5 mm (distal site) from the lesion epicenter.

Histological analysis

Toluidine blue staining (light microscopy)

Samples were fixed in 2.5% glutaraldehyde/0.1 M cacodylate buffer (pH 7.4) for 12 h, then washed in cacodylate buffer, post-fixed for 2 h in 1% OsO_4/0.1 M cacodylate buffer (pH 7.4), dehydrated in a graded alcohol series and acetone, and finally embedded in epoxy resin. Semi-thin sections (1 μm thick) were cut cross-sectionally from the injured nerve specimens from a site 5 mm distal to the lesion epicenter and at the lesion epicenter at 4 days, 3 weeks, and 12 weeks after the crush injury, and stained with toluidine blue (1%) for 20 min; the corresponding sections from intact nerve specimens were also examined. The stained sections were then examined under a light microscope (AxioCam 2; Carl Zeiss, Jena, Germany).

Uranyl acetate staining (electron microscopy)

Ultrathin sections (80 nm thick) were obtained from the intact and injured nerve specimens at the same sites and time points as for the light microscopic examination, and stained with uranyl acetate (4.7%) for 30 min and Reynold's lead citrate for 8 min. Micrographs from 20 random fields of 17×17 μm^2 were obtained under a transmission

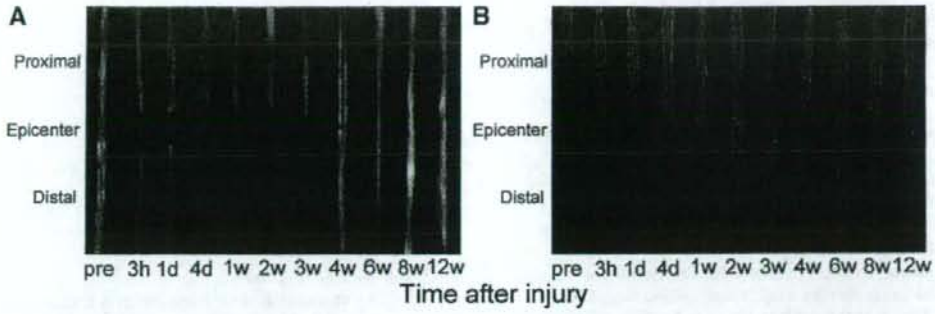

Fig. 1. FA map (A) and diffusion tensor tractography (B) of intact and injured sciatic nerves. For the tractography, the region of interest (ROI) was placed 5 mm proximal to the lesion epicenter. The FA value threshold was set at 0.4. In the DTT image constructed using this FA threshold value, the recovery process of the contused peripheral nerves could be clearly detected under the imaging parameters used.

electron microscope (JEOL model 1230; JEOL Ltd., Tokyo, Japan), by Digital Micrograph 3.3 (Gatan Inc., Warrendale, Pennsylvania, USA).

Quantitative analysis

Nerve samples were obtained at each of the ten time points used for diffusion tensor analysis, and subjected to quantitative determinations at the distal site, at which Wallerian degeneration/regeneration occurred. The following parameters were calculated for each nerve using the MCID system (Imaging Research, Inc., Toronto, Ontario, Canada): axon density, axon diameter, myelin sheath density, and myelin sheath thickness. Axon density was defined as axonal area/ total area, and myelin sheath density was defined as myelin sheath area/ total area in a fascicle in each nerve sample. The axon diameter and myelin sheath thickness of 40 randomly selected axons were

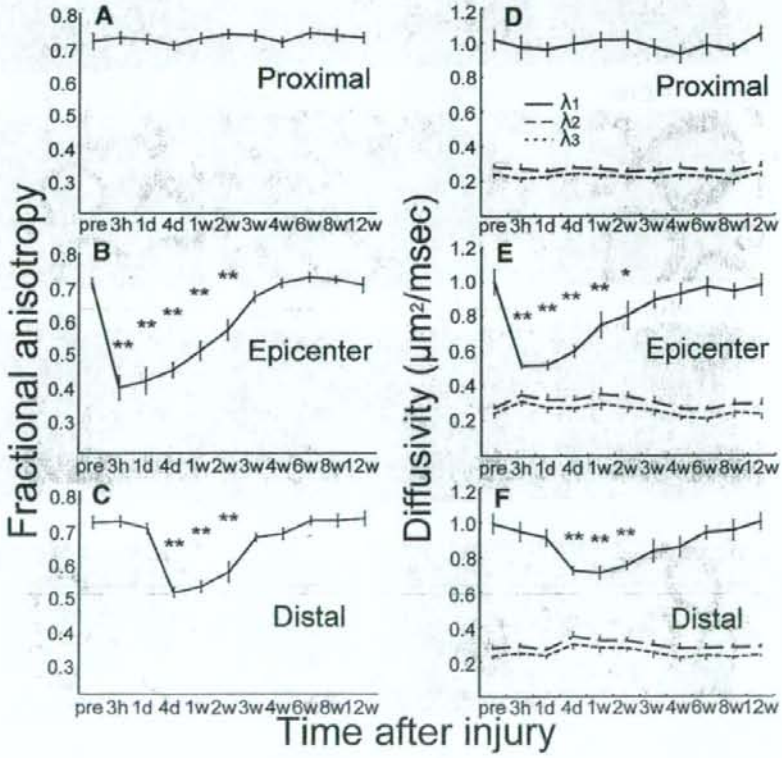

Fig. 2. Quantitative and temporal analysis of the FA values (A, proximal site; B, epicenter site; C, distal site), and eigenvalues (D, proximal site; E, epicenter site; F, distal site) ($n=10$ each). At the lesion epicenter, the FA value decreased sharply at 3 h and recovered gradually, reaching the pre-injury level by 3 weeks after the injury (B). At the distal site, while no significant change in the FA value was observed at 3 h or 1 day after the injury, a decrease was observed at 4 days, with gradual recovery thereafter to the pre-injury level by 3 weeks after the injury (C). The present model showed that both λ_2 and λ_3 were more constant than λ_1 (D–F), and that changes in FA values during the recovery after peripheral nerve injury depended mainly on λ_1, which represents the diffusivity along the longitudinal axis of the nerve. Statistical significance was determined to be $P<0.05$ using Dunnett's multiple comparison. Data represent the mean±SEM. *$P<0.05$; **$P<0.01$.

measured in each nerve sample. We also examined the changes in the distribution of the axon diameter after injury.

Behavioral analysis

Three different tests were used to assess the functional recovery after sciatic nerve injury. Ten rats were used for each functional evaluation. Each rat was examined at the same time-points used for the diffusion tensor analysis.

Leg muscle contraction test

The motor function of the lower extremities of the animals was evaluated using the leg muscle contraction test, in which isometric plantar flexion at the ankle is tested by pushing the sole until the toe touches the knee. A digital force gauge (Nidec-Shimpo Corp., Kyoto, Japan) was used for this test. The ratio of the degree of muscle contraction on the injured side to that on the contralateral sham-operated side was averaged.

Rota-rod test

The motor coordination of the animals was assessed using a rotating rod apparatus (Muromachi Kikai Co., Ltd., Tokyo, Japan) consisting of a plastic rod (9 cm in diameter) with a gritted surface, flanked by two large discs (50 cm in diameter) to prevent interference from other animals, at a height of 20 cm from the floor. The experimental rat was placed on the rod, and the rod was rotated at a speed of 15 rpm, following acclimation sessions (3 trials each at 5 and 10 rpm). The latency period until the rats fell off the apparatus was monitored for 180 s.

von Frey filament test

The mechanical sensitivity, which is the capacity of a sense organ to respond to mechanical stimulation, of the animals was tested using von Frey filaments (North Coast Medical Inc., Morgan Hill, California, USA) with calibrated bending forces (Tamae et al., 2005). Rats were placed individually in an acrylic cap (12 cm in diameter, 7 cm in height, and weighing 256 g) with a wire mesh bottom. After the rats

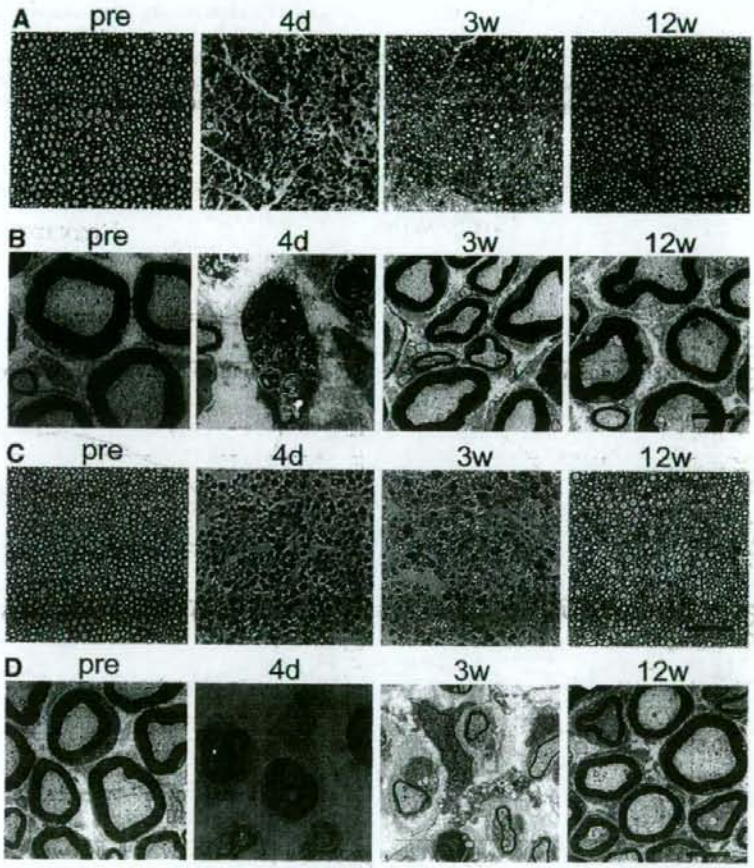

Fig. 3. Histological changes in the peripheral nerves at the lesion epicenter and at the distal site. Sections of 1 μm (A), stained with toluidine blue, and 80 nm (B), stained with uranyl acetate, were obtained from the lesion epicenter. Loss of axons and myelin debris arising from demyelination were observed 4 days after the injury (A). The phagocytosis of myelin debris by macrophages was observed (B). At 3 weeks after the injury, as the amount of myelin debris and number of macrophages decreased, myelinated axons became prominent. At 12 weeks after the injury, a similar number of myelinated axons to that in the pre-injury sciatic nerve was observed (A, B). Sections of 1 μm (C) stained with toluidine blue, and 80 nm (D) stained with uranyl acetate, were obtained from the site distal to the lesion epicenter. The series indicates that the axonal structures began to disintegrate within 4 days after the injury, then the axons began to regenerate by 3 weeks after the injury, and reached almost the pre-injury level of maturity by the end of the experimental period (C). Myelin debris was frequently detected 4 days after the injury. Macrophage recruitment, presumably for phagocytosis of the myelin debris, and very small axons within thin myelin sheaths were observed 3 weeks after the injury, followed by the formation of myelinated axons (D). (AX, axon; MS, myelin sheath; SC, Schwann cell; M, macrophage; scale bar, (A, C) 50 μm, (B, D) 5 μm).

had adapted to the testing environment for 60 min, the von Frey filaments were pressed perpendicularly against the plantar skin and held for 3–5 s with the filaments slightly buckled. Lifting of the paw was recorded as a positive response. The filaments were applied to the point of bending, six times each, to the plantar surface of the left and right hind paw, i.e., for a total of 12 times per rat, at intervals of 5 s; the next lightest filament was chosen for each subsequent measurement. The paw withdrawal threshold was taken as the lowest force that caused 100% withdrawals, and was considered the mechanical nociceptive threshold. The threshold ratio of the contralateral sham-operated side to that of the injured side was averaged.

Statistical analysis

All values were presented as the mean ± standard error of the mean (SEM). Statistical significance was determined as $P<0.05$ using Dunnett's multiple comparison. Pearson's correlation coefficients were calculated to determine the correlations between the histological/functional parameters and the diffusion imaging parameters. The SPSS statistical analysis software (version 16.0) was used for the analyses (SPSS Japan Inc., Tokyo, Japan).

Results

Diffusion tensor tractography and fractional anisotropy of injured peripheral nerves

We generated FA maps and delineated DTT images of the rat sciatic nerve for 12 weeks after contusive injury. On the FA maps (Fig. 1A), a sharp decrease in the intensity at the lesion epicenter was noted 3 h after the injury; thereafter, the intensity recovered gradually, reaching the pre-injury level by 4 weeks after the injury. At the distal site, the intensity was still preserved at both 3 h and 1 day; however, it was significantly decreased 4 days after the injury, and recovered gradually thereafter, reaching pre-injury levels by 4 weeks after the injury. Since tracking of the sciatic nerve depends on the selected FA threshold, at which the tracking is stopped, we also delineated DTT images of the sciatic nerves for 12 weeks after the injury using different FA thresholds: 0.25, 0.3, 0.4, 0.5, 0.6, 0.7, or 0.75 (Supplementary Figs. 1A–G). We found that the DTT images obtained using a FA threshold value of 0.4 (Fig. 1B) clearly showed the recovery process of the contused nerves. At 3 h after the injury, the fibers from the designated proximal site could not be tracked beyond the lesion epicenter, and fiber tracking could not proceed beyond the lesion epicenter until 1 day after the injury. On the other hand, a few fibers could be tracked distally by 4 days after the injury. The tractography revealed a return of the tracking parameters to the pre-injury levels, close those of the normal sciatic nerve, by 3 weeks after the injury.

Table 2
Correlations of the diffusion imaging parameters (Pearson's r) with the histological parameters

	Axon density	Axon diameter	Myelin density	Myelin thickness
FA	0.8618****	0.9166****	0.2387	−0.6941*
λ_1	0.9605****	0.9607****	0.4449	−0.5780

* $P<0.05$.
**** $P<0.001$.

To analyze the changes in the anisotropy of the injured sciatic nerves by DTI, we measured the FA values for 12 weeks after the injury. There were no significant changes in the FA value at the proximal site at any time point examined (Fig. 2A). In contrast, at the lesion epicenter, a sharp decrease in the FA value was observed 3 h after the injury, which then recovered gradually, reaching the pre-injury level by 3 weeks after the injury (Fig. 2B). In the images of the distal site, while no significant change in the FA value was observed at 3 h or 1 day, a decrease in the FA value was observed at 4 days, followed by gradual recovery thereafter, to the pre-injury level by 3 weeks after the injury (Fig. 2C).

We next analyzed the individual eigenvalues. The first eigenvalue (λ_1), which represents the diffusivity along the longitudinal axis of the nerve, was substantially higher than the second (λ_2) and third (λ_3) eigenvalues, which represent the diffusivity in directions perpendicular to the longitudinal axis. These radial diffusivities (λ_2 and λ_3) were much lower than the diffusivity value along the axis of the tract (λ_1). Thus, the present model showed that both λ_2 and λ_3 were more constant than λ_1 (Figs. 2D–F), and that the changes in the FA values after peripheral nerve injury depended mainly on λ_1, which represents the diffusivity along the longitudinal axis of the nerve.

Fig. 4. Quantitative and temporal analysis of the axon density (myelinated axon area / total sectioned nerve area) (A), axon diameter (B), myelin sheath density (myelin sheath area / total sectioned nerve area) (C), and myelin sheath thickness (D) at the nerve site distal to the lesion epicenter ($n=10$ each). Statistical significance was determined to be $P<0.05$ using Dunnett's multiple comparison. Data represent the mean ± SEM. *$P<0.05$; **$P<0.01$.

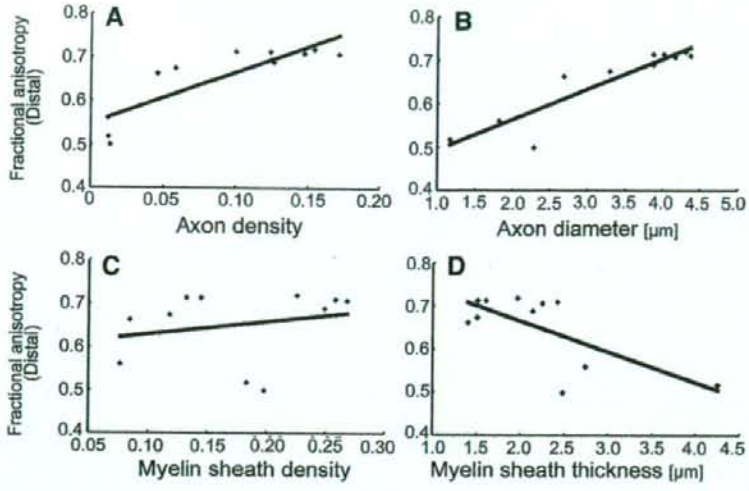

Fig. 5. Correlations between FA values and histological parameters. The FA values at the distal site were strongly correlated with each of the axonal parameters (A, Axon density, $r=0.8618$, $P=0.0006$; B, Axon diameter, $r=0.9166$, $P=0.0001$; C, Myelin sheath density, $r=0.2387$, $P=0.4796$; D, Myelin sheath thickness, $r=-0.6941$, $P=0.0178$).

Histological changes in the injured peripheral nerves

To examine the histological changes in the axons and myelin sheaths in detail, we performed toluidine blue and uranyl acetate staining of the nerves at the lesion epicenter and the distal site. At the lesion epicenter, axon loss and myelin debris arising from demyelination were observed 4 days after the injury (Fig. 3A). Consistent with these findings, EM examination revealed myelin debris being phagocytosed by macrophages (Fig. 3B). Subsequently, 3 weeks after the injury, as the amount of myelin debris and number of macrophages decreased, and myelinated axons began to appear prominently. At 12 weeks after the injury, myelinated axons similar in appearance and number to those in the pre-injury sciatic nerve were observed (Figs. 3A and B). At the distal site 4 days after the injury, more myelin debris and greater irregularity of the myelin sheaths were observed compared with the lesion epicenter (Figs. 3C and D), and fewer phagocytic macrophages were detected than at the lesion epicenter. A few regenerating axons, which appeared to be myelinated axons of smaller caliber with a thinner myelin sheath compared to normal axons, could be detected at 3 weeks, and these axons gradually reached the pre-injury level of maturity by 12 weeks after the injury (Fig. 3C). Three weeks after the injury, there was still a little myelin debris, which was being phagocytosed by macrophages, and a few small axons with thin myelin sheaths. These immature myelinated axons became progressively more mature and prominent with a thick myelin sheath, and the regenerated axons appeared similar to the axons observed pre-injury, by 12 weeks after the injury (Fig. 3D).

To analyze these changes quantitatively, we focused on the distal site, at which the Wallerian degeneration and regeneration could be clearly observed. We measured the number of axons, and the ratio of the myelinated axon area to the total sectioned nerve area as the axon density. The axon density decreased immediately after the nerve injury, reaching a minimum between 4 days and 2 weeks after the injury, and recovered gradually thereafter (Fig. 4A).

At this distal site, we also measured the ratio of the myelin sheath area to the total sectioned nerve area as the myelin sheath density. The myelin sheath density decreased gradually, reaching a minimum value 2 weeks after the injury, and began to recover thereafter (Fig. 4C). In addition, the axon diameter and myelin sheath thickness were measured in ultrathin (80 nm) sections under the electron microscope. No significant change in the axon diameter was noted until 1 day after the injury. Thereafter, with the swelling and degeneration of the myelin sheath, the axon diameter began to decrease, reaching a minimum at 1 week, and then recovered to the pre-injury level by 6 weeks after the injury (Fig. 4B). Furthermore, there was an obvious change in the pattern of axon diameter distribution pre and post injury (Supplementary Fig. 2). In contrast, the myelin sheath thickness increased to its maximum value at

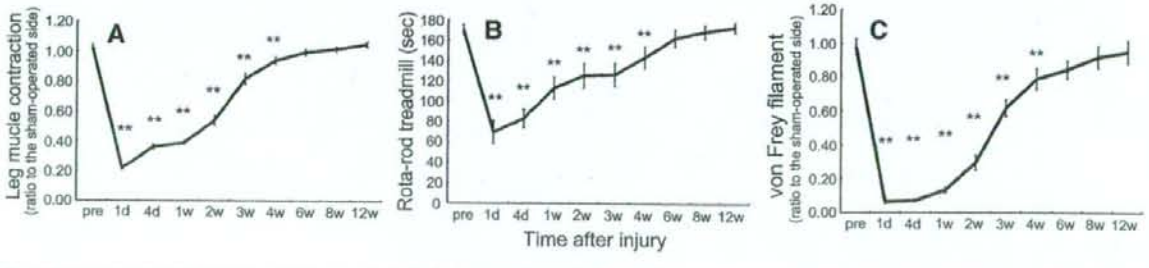

Fig. 6. Temporal analysis of the recovery of motor function in the lower extremities by the leg muscle contraction test (A), of motor coordination by the Rota-rod test (B), and of mechanical sensitivity by the von Frey filament test (C) for 12 weeks after contusion injury of the nerve. All three behavioral evaluations revealed functional recovery within 6 weeks of the nerve injury in this experimental model. Statistical significance was determined to be $P<0.05$ using Dunnett's multiple comparison. Data represent the mean ± SEM. *$P<0.05$; **$P<0.01$.

Table 3
Correlations of the diffusion imaging parameters (Pearson's r) with the functional parameters

	Leg muscle contraction	Rota-rod treadmill	von Frey filament
FA	0.9851****	0.9451****	0.9667****
λ_1	0.9591****	0.9695****	0.9355****

**** $P<0.001$.

1 week, due to swelling of the degenerated myelin sheath, and decreased gradually thereafter, accompanied by the disappearance of myelin debris. Regenerating axons with a thin myelin sheath began to appear by 2–3 weeks after the injury. A few more small, regenerating axons with a myelin sheath thinner than that observed pre-injury were detected at 3–8 weeks, and their number approached the pre-injury level by 12 weeks, accompanied by maturation of the myelin sheaths (Fig. 4D).

Almost all the histological axonal parameters were correlated with the FA and λ_1 values at the distal site. The FA value, a parameter used to construct the DTT, was most strongly correlated with the axon density and axon diameter ($P<0.001$) (Table 2 and Fig. 5).

Functional recovery after peripheral nerve injury

We next investigated whether the changes in FA values and histological parameters were associated with functional recovery, using three different behavioral tests. To evaluate the recovery of motor function, we measured the degree of leg muscle contraction, and assessed the forelimb-hindlimb motor coordination using the Rota-rod treadmill test. Both of these tests showed the full recovery of motor function by 6 weeks after the injury ($P<0.05$) (Figs. 6A and B). Sensory function was evaluated using the von Frey filament test. Marked impairment was observed 1 day after the injury, after which the values gradually improved, returning to pre-injury levels by 6 weeks ($P<0.05$) (Fig. 6C). Thus, all three behavioral evaluations revealed functional recovery within 6 weeks in this experimental model.

The FA and λ_1 values at the lesion epicenter showed strong correlations with each of the aforementioned functional parameters ($P<0.001$) (Table 3 and Fig. 7).

Discussion

Methodological considerations

Beaulieu et al. reported that Wallerian degeneration after peripheral nerve injury reduces the anisotropy of water diffusion (Beaulieu et al., 1996; Stanisz et al., 2001). Their findings indicated that DTT might be useful for depicting the changes in anisotropy after peripheral nerve injury, and thus has tremendous potential as a tool for diagnosing peripheral nerve injury. However, although several preliminary studies for the DTT of peripheral nerves have been performed (Hiltunen et al., 2005; Meek et al., 2006; Skorpil et al., 2004), none has fully explored the potential of the DTI technology, especially its ability to depict the degeneration and regeneration of peripheral nerves after injury.

To apply DTT as a novel clinical tool for evaluating peripheral nerve injury, it is first necessary to acquire accurate data for visualizing Wallerian degeneration and regeneration. In the present study, we used a highly reproducible model, in which the rat sciatic nerve was subjected to contusive injury using an aneurysm clip, with a constant holding force. The histological changes in our model were similar to those in previously reported models of axonotmesis (Bridge et al., 1994; Varejao et al., 2004), in which spontaneous regeneration at a distal nerve section and functional recovery were also observed. We used 7.0-Tesla MRI to obtain the images, employing a conventional spin-echo protocol rather than echo planar imaging, to minimize distortion of the images due to phase errors accumulation during the data acquisition. To reduce motion artifacts, the MR images of excised nerves were obtained. Since previous studies have demonstrated degradation of the diffusion anisotropy in excised models (Madi et al., 2005; Matsuzawa et al., 1995), we captured all the images immediately after dissection of the sciatic nerve.

Interpretation of the diffusion anisotropy

The FA value at the lesion epicenter decreased immediately after the injury. On the other hand, at the distal site, while no significant change in the FA value was observed at 3 h or 1 day after the injury, a significant decrease in the value was observed 4 days after the injury. These results were consistent with the histological findings, which showed that the axons and myelin were preserved in the nerve segment distal to the lesion epicenter up to 1 day after the injury, with disintegration of the axonal structures and demyelination (Wallerian degeneration), being observed 4 days after the injury. The perineurium, the sheath of connective tissue that surrounds each neural fascicle, was still preserved (Lundborg, 2004; Sunderland, 1991) and regulated the diffusivity. As a result, while the axon density decreased to nearly zero (Fig. 4A) in the preserved fascicles, a less than 30% drop in the FA value was observed at 4 days after the injury. Thereafter, the FA value recovered gradually, reaching its pre-injury level by 3 weeks after the injury, when a few regenerating axons could be detected; that is, the FA value at the distal site returned to its pre-injury level prior to the histological recovery. Furthermore, the FA values at the lesion epicenter during recovery showed extremely strong correlations with each of the functional parameters examined.

To clarify the relevance of the changes in the FA values after peripheral nerve injury, we examined the correlations between the FA values and the quantitative changes in axonal properties. The FA values of the peripheral nerves were more strongly correlated with the axonal density and diameter than with the myelin density and thickness. These findings support the theories that the axonal

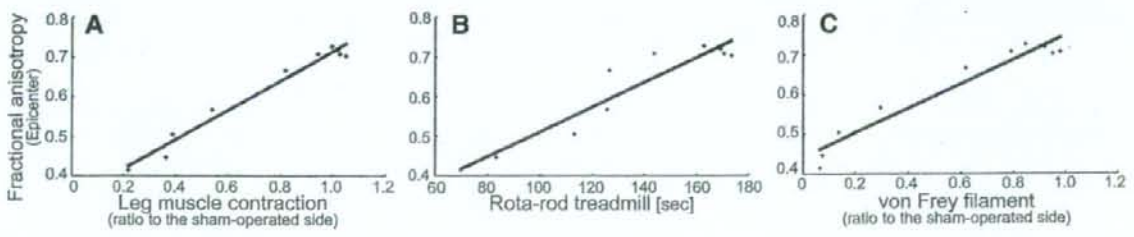

Fig. 7. Correlations between FA values and functional parameters. The FA values at the lesion epicenter were strongly correlated with each of the functional parameters (A, leg muscle contraction, $r=0.9851$, $P=0.000001$; B, Rota-rod treadmill, $r=0.9451$, $P=0.00004$; C, von Frey filament, $r=0.9667$, $P=0.000005$).

membranes play a major role in the anisotropic water diffusion in neural fibers (Beaulieu, 2002; Takahashi et al., 2002) and that myelination can modulate the degree of anisotropy (Gulani et al., 2001). The changes in the FA values after nerve injury mainly depended on λ_1, i.e., the axial diffusivity, consistent with the idea that water molecules preferentially diffuse along the longitudinal axis of axons, and degradation of the axonal cylinders would cause a loss of axial diffusivity. In addition, the absence of any significant change in the radial diffusivities (λ_2 and λ_3) might be explained by the present imaging conditions not being adequate to detect subtle changes of the radial diffusivities, which were significantly smaller than the axial diffusivity.

Potential clinical uses

Because it is difficult to distinguish peripheral nerves clearly from the surrounding tissues in conventional T1- and T2-weighted images, visualization of the Wallerian degeneration and regeneration of peripheral nerves after injury by MRI has been a challenge (Bendszus et al., 2002; Bendszus and Stoll, 2003; Bendszus et al., 2005; Filler et al., 1993; Howe et al., 1992; Kikuchi et al., 2003). In the present study, we were able to visualize these changes in peripheral nerves using DTI, and good correlations were found between the recovery as assessed by the changes in FA values and by histological and functional parameters. These findings support the applicability of DTI to the diagnosis of peripheral nerve injuries and monitoring of pathological conditions, to obtain information about the early phases of recovery in a clinical context.

We note that fiber tracking can sometimes terminate abruptly, because sharp bending or branching of the nerve can reduce the anisotropy below the tracking threshold (Hiltunen et al., 2005); therefore, the appropriate positioning and selection of a segment without branches will be critical, unless the spatial or angular resolution of the diffusion is greatly increased. In addition, although we have demonstrated the tracking and analysis of a straight sciatic nerve from the rat, which measures 1–1.5 mm in diameter and corresponds to the diameter of cutaneous nerves in humans, in voxels 0.31 mm in size, it is also important to keep in mind that the voxels forming the basis of the tracking are considerably larger than any individual axonal tract (Fujiyoshi et al., 2007).

We attempted to perform an in vivo study in a live model using smaller nerves to determine the feasibility of this method for clinical use (see Supplementary Materials), and we were able to demonstrate the recovery process of contused nerves in the same animal by tractography (Supplementary Fig. 3). Thus, DTT of the peripheral nerves could become an innovative tool for the evaluation of peripheral nerve injury, if applied correctly and with a clear understanding of its properties and limitations.

Acknowledgments

This work was supported by grants from the Leading Project for Realization of Regenerative Medicine from the Ministry of Education, Culture, Sports, Science and Technology (MEXT), Japan, from the Japan Science and Technology Corporation (JST), and from the General Insurance Association of Japan. This work was also supported by a Keio University grant-in-aid for encouragement of young medical scientists, by grants-in-aid for scientific research of MEXT, Japan, and by a grant-in-aid from the 21st Century COE Program of MEXT, Japan to Keio University. We thank Tokuko Harada and Hisako Takeuchi for tender animal care, Toshihiro Nagai for technical assistance with the electron microscope, and to all the other members of the spinal cord injury research team at Keio University School of Medicine for their enthusiastic discussions, encouragement, and invaluable comments on this study.

The authors declare no competing financial interests.

Appendix A. Supplementary data

Supplementary data associated with this article can be found, in the online version, at doi:10.1016/j.neuroimage.2008.09.022.

References

Basser, P.J., Mattiello, J., LeBihan, D., 1994. MR diffusion tensor spectroscopy and imaging. Biophys. J. 66, 259–267.
Beaulieu, C., 2002. The basis of anisotropic water diffusion in the nervous system – a technical review. NMR Biomed. 15, 435–455.
Beaulieu, C., Does, M.D., Snyder, R.E., Allen, P.S., 1996. Changes in water diffusion due to Wallerian degeneration in peripheral nerve. Magn. Reson. Med. 36, 627–631.
Bendszus, M., Stoll, G., 2003. Caught in the act: in vivo mapping of macrophage infiltration in nerve injury by magnetic resonance imaging. J. Neurosci. 23, 10892–10896.
Bendszus, M., Koltzenburg, M., Wessig, C., Solymosi, L., 2002. Sequential MR imaging of denervated muscle: experimental study. AJNR Am. J. Neuroradiol. 23, 1427–1431.
Bendszus, M., Wessig, C., Schutz, A., Horn, T., Kleinschnitz, C., Sommer, C., Misselwitz, B., Stoll, G., 2005. Assessment of nerve degeneration by gadofluorine M-enhanced magnetic resonance imaging. Ann. Neurol. 57, 388–395.
Bridge, P.M., Ball, D.J., Mackinnon, S.E., Nakao, Y., Brandt, K., Hunter, D.A., Hertl, C., 1994. Nerve crush injuries – a model for axonotmesis. Exp. Neurol. 127, 284–290.
Conturo, T.E., Lori, N.F., Cull, T.S., Akbudak, E., Snyder, A.Z., Shimony, J.S., McKinstry, R.C., Burton, H., Raichle, M.E., 1999. Tracking neuronal fiber pathways in the living human brain. Proc. Natl. Acad. Sci. U. S. A. 96, 10422–10427.
Filler, A.G., Howe, F.A., Hayes, C.E., Kliot, M., Winn, H.R., Bell, B.A., Griffiths, J.R., Tsuruda, J.S., 1993. Magnetic resonance neurography. Lancet 341, 659–661.
Filler, A.G., Maravilla, K.R., Tsuruda, J.S., 2004. MR neurography and muscle MR imaging for image diagnosis of disorders affecting the peripheral nerves and musculature. Neurol. Clin. 22, 643–682 vi-vii.
Fujiyoshi, K., Yamada, M., Nakamura, M., Yamane, J., Katoh, H., Kitamura, K., Kawai, K., Okada, S., Momoshima, S., Toyama, Y., Okano, H., 2007. In vivo tracing of neural tracts in the intact and injured spinal cord of marmosets by diffusion tensor tractography. J. Neurosci. 27, 11991–11998.
Gulani, V., Webb, A.G., Duncan, I.D., Lauterbur, P.C., 2001. Apparent diffusion tensor measurements in myelin-deficient rat spinal cords. Magn Reson Med 45, 191–195.
Hiltunen, J., Suortti, T., Arvela, S., Seppa, M., Joensuu, R., Hari, R., 2005. Diffusion tensor imaging and tractography of distal peripheral nerves at 3 T. Clin. Neurophysiol. 116, 2315–2323.
Howe, F.A., Filler, A.G., Bell, B.A., Griffiths, J.R., 1992. Magnetic resonance neurography. Magn. Reson. Med. 28, 328–338.
Kato, N., Nemoto, K., Nakanishi, K., Morishita, R., Kaneda, Y., Uenoyama, M., Ikeda, T., Fujikawa, K., 2005. Nonviral HVJ (hemagglutinating virus of Japan) liposome-mediated retrograde gene transfer of human hepatocyte growth factor into rat nervous system promotes functional and histological recovery of the crushed nerve. Neurosci. Res. 52, 299–310.
Kikuchi, Y., Nakamura, T., Takayama, S., Horiuchi, Y., Toyama, Y., 2003. MR imaging in the diagnosis of denervated and reinnervated skeletal muscles: experimental study in rats. Radiology 229, 861–867.
Lundborg, G., 2004. Nerve Injury and Repair, second ed. Elsevier, Philadelphia.
Mac Donald, C.L., Dikranian, K., Bayly, P., Holtzman, D., Brody, D., 2007a. Diffusion tensor imaging reliably detects experimental traumatic axonal injury and indicates approximate time of injury. J. Neurosci. 27, 11869–11876.
Mac Donald, C.L., Dikranian, K., Song, S.K., Bayly, P.V., Holtzman, D.M., Brody, D.L., 2007b. Detection of traumatic axonal injury with diffusion tensor imaging in a mouse model of traumatic brain injury. Exp. Neurol. 205, 116–131.
Madi, S., Hasan, K.M., Narayana, P.A., 2005. Diffusion tensor imaging of in vivo and excised rat spinal cord at 7 T with an icosahedral encoding scheme. Magn. Reson. Med. 53, 118–125.
Masutani, Y., Aoki, S., Abe, O., Hayashi, N., Otomo, K., 2003. MR diffusion tensor imaging: recent advance and new techniques for diffusion tensor visualization. Eur. J. Radiol. 46, 53–66.
Matsuzawa, H., Kwee, I.L., Nakada, T., 1995. Magnetic resonance axonography of the rat spinal cord: postmortem effects. J. Neurosurg. 83, 1023–1028.
Meek, M.F., Stenekes, M.W., Hoogduin, H.M., Nicolai, J.P., 2006. In vivo three-dimensional reconstruction of human median nerves by diffusion tensor imaging. Exp. Neurol. 198, 479–482.
Mori, S., Zhang, J., 2006. Principles of diffusion tensor imaging and its applications to basic neuroscience research. Neuron 51, 527–539.
Pierpaoli, C., Basser, P.J., 1996. Toward a quantitative assessment of diffusion anisotropy. Magn. Reson. Med. 36, 893–906.
Skorpil, M., Karlsson, M., Nordell, A., 2004. Peripheral nerve diffusion tensor imaging. Magn. Reson. Imaging 22, 743–745.
Song, S.K., Sun, S.W., Ju, W.K., Lin, S.J., Cross, A.H., Neufeld, A.H., 2003. Diffusion tensor imaging detects and differentiates axon and myelin degeneration in mouse optic nerve after retinal ischemia. Neuroimage 20, 1714–1722.
Stanisz, G.J., Midha, R., Munro, C.A., Henkelman, R.M., 2001. MR properties of rat sciatic nerve following trauma. Magn. Reson. Med. 45, 415–420.
Stejskal, E.O., Tanner, J.E., 1965. Spin diffusion measurements: spin echoes in the presence of a time dependent field gradient. J. Chem. Phys. 42, 288–292.
Sun, S.W., Liang, H.F., Cross, A.H., Song, S.K., 2008. Evolving Wallerian degeneration after transient retinal ischemia in mice characterized by diffusion tensor imaging. Neuroimage 40, 1–10.
Sunderland, S.S., 1991. Nerve Injuries and Their Repair: a Critical Appraisal. Churchill Livingstone, New York.
Takahashi, M., Hackney, D.B., Zhang, G., Wehrli, S.L., Wright, A.C., O'Brien, W.T., Uematsu, H., Wehrli, F.W., Selzer, M.E., 2002. Magnetic resonance microimaging of

intraaxonal water diffusion in live excised lamprey spinal cord. Proc. Natl. Acad. Sci. U. S. A. 99, 16192–16196.
Tamae, A., Nakatsuka, T., Koga, K., Kato, G., Furue, H., Katafuchi, T., Yoshimura, M., 2005. Direct inhibition of substantia gelatinosa neurones in the rat spinal cord by activation of dopamine D2-like receptors. J. Physiol. 568, 243–253.
Tuch, D.S., Wedeen, V.J., Dale, A.M., George, J.S., Belliveau, J.W., 2001. Conductivity tensor mapping of the human brain using diffusion tensor MRI. Proc. Natl. Acad. Sci. U. S. A. 98, 11697–11701.
Varejao, A.S., Cabrita, A.M., Meek, M.F., Bulas-Cruz, J., Melo-Pinto, P., Raimondo, S., Geuna, S., Giacobini-Robecchi, M.G., 2004. Functional and morphological assessment of a standardized rat sciatic nerve crush injury with a non-serrated clamp. J. Neurotrauma 21, 1652–1670.
Wessig, C., Jestaedt, L., Sereda, M.W., Bendszus, M., Stoll, G., 2008. Gadofluorine M-enhanced magnetic resonance nerve imaging: comparison between acute inflammatory and chronic degenerative demyelination in rats. Exp. Neurol. 210, 137–143.

ARTHRITIS & RHEUMATISM
Vol. 58, No. 9, September 2008, pp 2764–2775
DOI 10.1002/art.23805

The Distinct Role of the Runx Proteins in Chondrocyte Differentiation and Intervertebral Disc Degeneration

Findings in Murine Models and in Human Disease

Shingo Sato,[1] Ayako Kimura,[1] Jerfi Ozdemir,[2] Yoshinori Asou,[1] Makiko Miyazaki,[1] Tetsuya Jinno,[1] Keisuke Ae,[1] Xiuyun Liu,[2] Mitsuhiko Osaki,[3] Yasuhiro Takeuchi,[4] Seiji Fukumoto,[5] Hiroshi Kawaguchi,[5] Hirotaka Haro,[6] Ken-ichi Shinomiya,[1] Gerard Karsenty,[2] and Shu Takeda[1]

Objective. **Runx2 is a transcription factor that regulates chondrocyte differentiation. This study was undertaken to address the role of the different Runx proteins (Runx1, Runx2, or Runx3) in chondrocyte differentiation using chondrocyte-specific *Runx*–transgenic mice, and to study the importance of the QA domain of Runx2, which is involved in its transcriptional activation.**

Methods. ***Runx*** **expression was analyzed in the mouse embryo by in situ hybridization. Overexpression of *Runx*1, *Runx*2 (lacking the QA domain [ΔQA]), or *Runx*3 was induced in chondrocytes in vivo, to produce α(1)II-*Runx*1, α(1)II-*Runx*2ΔQA, and α(1)II-*Runx*3 mice, respectively, for histologic and molecular analyses. Runx expression was also examined in an experimental mouse model of mechanical stress–induced intervertebral disc (IVD) degeneration and in human patients with IVD degeneration.**

Results. ***Runx*1 expression was transiently observed in condensations of mesenchymal cells, whereas *Runx*2 and *Runx*3 were robustly expressed in prehypertrophic chondrocytes. Similar to α(1)II-*Runx*2 mice, α(1)II-*Runx*2ΔQA and α(1)II-*Runx*3 mice developed ectopic mineralization of cartilage, but this was less severe in the α(1)II-*Runx*2ΔQA mice. In contrast, α(1)II-*Runx*1 mice displayed no signs of ectopic mineralization. Surprisingly, α(1)II-*Runx*1 and α(1)II-*Runx*2 mice developed scoliosis due to IVD degeneration, characterized by an accumulation of extracellular matrix and ectopic chondrocyte hypertrophy. During mouse embryogenesis, Runx2, but not Runx1 or Runx3, was expressed in the IVDs. Moreover, both in the mouse model of IVD degeneration and in human patients with IVD degeneration, there was significant up-regulation of Runx2 expression.**

Conclusion. **Each Runx protein has a distinct, yet overlapping, role during chondrocyte differentiation. Runx2 contributes to the pathogenesis of IVD degeneration.**

Cells of the chondrocyte lineage play critical roles at several stages of endochondral ossification (1). Chondrocytes are the first skeletal-specific cell type that can be identified in the condensations of mesenchymal cells that precede the development of skeletal elements (2).

Supported by Grant-in-Aid for Scientific Research grants from the Japan Society for the Promotion of Science to Drs. Asou, Jinno, Ae, Shinomiya, and Takeda, and by 21st Century Center of Excellence Program grants from the Ministry of Education, Culture, Sports, Science, and Technology of Japan to Drs. Shinomiya and Takeda. Dr. Takeda's work also was supported by grants from Uehara Memorial Foundation. Dr. Karsenty's work was supported by a grant from the NIH.

[1]Shingo Sato, MD, PhD, Ayako Kimura, MS, Yoshinori Asou, MD, PhD, Makiko Miyazaki, MD, Tetsuya Jinno, MD, PhD, Keisuke Ae, MD, PhD, Ken-ichi Shinomiya, MD, PhD, Shu Takeda, MD, PhD: Tokyo Medical and Dental University, Tokyo, Japan; [2]Jerfi Ozdemir, BSc, MBA, Xiuyun Liu, Gerard Karsenty, MD, PhD (current address: Columbia University, New York, New York): Baylor College of Medicine, Houston, Texas; [3]Mitsuhiko Osaki, PhD: Tottori University, Tottori, Japan; [4]Yasuhiro Takeuchi, MD, PhD: Toranomon Hospital, Tokyo, Japan; [5]Seiji Fukumoto, MD, PhD, Hiroshi Kawaguchi, MD, PhD: University of Tokyo, Tokyo, Japan; [6]Hirotaka Haro, MD, PhD: University of Yamanashi, Yamanashi, Japan.

Dr. Sato, Ms Kimura, and Ms Ozdemir contributed equally to this work.

Dr. Takeuchi has received speaking fees from Eisai Company, Ltd. and Teijin Pharma, Ltd. (less than $10,000 each).

Address correspondence and reprint requests to Shu Takeda, MD, PhD, Department of Orthopedic Surgery, Tokyo Medical and Dental University, 1-5-45 Yushima, Bunkyo-ku, Tokyo 113-8519, Japan. E-mail: shu-tky@umin.ac.jp.

Submitted for publication February 14, 2008; accepted in revised form May 29, 2008.

At these initial stages of development, chondrocytes actively divide or proliferate, and express a specific molecular marker, α1(II) collagen. Around embryonic day 14.5 of mouse development, chondrocytes in the center of these mesenchymal condensations become hypertrophic and form 2 distinct cell populations: prehypertrophic chondrocytes that continue to express α1(II) collagen, and hypertrophic chondrocytes that exit the cell cycle and express α1(X) collagen as a specific molecular marker (3). Hypertrophic chondrocytes replace the extracellular matrix with one that is permissive to vascular invasion; this allows the entry of osteoblastic cells. Subsequently, and at either end of a given skeletal element, chondrocytes organize into columns, forming growth-plate cartilage, which is responsible for linear skeletal growth (1).

Major progress has been made, over the last decade, in our understanding of the transcriptional control of chondrocyte differentiation (2). Work in multiple laboratories has established the critical role of Sox9 (4), along with Sox5 and Sox6 (5), in the differentiation of nonhypertrophic chondrocytes. Meanwhile, Runx2 (6–8), together with Runx3 (9), has been shown to favor chondrocyte hypertrophy. We previously demonstrated that continuous expression of *Runx*2 in nonhypertrophic chondrocytes (herein comprising the α(1)II-*Runx*2 group of mice) led to the development of ectopic hypertrophy of chondrocytes, followed by bone formation (7).

Runx1, the other member of the Runx family, shares a highly homologous DNA binding domain, the runt domain, with Runx2 and Runx3. There are also homologous regions N-terminal to the runt domain that are common to Runx1, Runx2, and Runx3. Although the last 5 amino acids of all 3 Runx proteins are identical, Runx2 possesses a unique QA domain composed of a stretch of Q and A residues (10).

Currently, it is unknown whether a functional hierarchy exists among Runx2, Runx3, and Runx1 (10). In addition, the significance of the QA domain of Runx2 in inducing chondrocyte differentiation remains to be elucidated. Therefore, in the present study, we generated transgenic mice that overexpressed *Runx*1 or *Runx*3 or lacked a QA domain in *Runx*2 (comprising the α(1)II-*Runx*1, α(1)II-*Runx*3, and α(1)II-*Runx*2ΔQA groups of mice, respectively). The mice were generated using the identical promoter/enhancer construct that we have previously used to specifically express *Runx*2 in chondrocytes (7).

Our results showed that all 3 *Runx* genes were expressed in cells of the chondrocyte lineage, but each functioned differently in these cells. The α(1)II-*Runx*3 and α(1)II-*Runx*2ΔQA mice developed ectopic differentiation of hypertrophic chondrocytes in chondrocostal cartilage, albeit to a lesser extent in the α(1)II-*Runx*2ΔQA mice. Surprisingly, α(1)II-*Runx*1 and α(1)II-*Runx*2 mice exhibited a kyphotic deformity of the vertebrae due to intervertebral disc (IVD) degeneration. We therefore studied an experimental mouse model of mechanical stress–induced IVD degeneration, which showed that Runx2, but not Runx1 or Runx3, was induced in the degenerated IVD. In addition, in human patients with IVD degeneration, we found that Runx2 expression was up-regulated, thus substantiating the pathophysiologic importance of Runx2 in the development of IVD degeneration in humans. This study illustrates the specific and distinct role of the *Runx* genes in physiologic conditions such as chondrocytic differentiation, and in pathologic conditions such as IVD degeneration.

MATERIALS AND METHODS

Generation of transgenic mice and analysis of transgene expression. The α1(II)-*Runx*1, α1(II)-*Runx*3, and α1(II)-*Runx*2ΔQA transgenes were obtained by subcloning *Runx*1, *Runx*3, or *Runx*2ΔQA complementary DNA (cDNA) (11) into an α1(II) collagen–expressing chondrocyte–specific promoter cassette (7). Transgenic founders were obtained by pronuclear injection into C57BL/6 oocytes, as previously described (7). We thus obtained multiple lines of transgenic mice with identical phenotypes in all groups except for the α1(II)-*Runx*3 mice. The *Runx*2-deficient mice were a generous gift from Dr. M. Owen (12). Wild-type (WT) mice were purchased from Jackson Laboratories (Bar Harbor, ME).

The genotypes of the mice were determined by polymerase chain reaction (PCR). (A list of the PCR primer sequences is available upon request from the corresponding author.) Chondrocyte RNA was extracted from chondrocostal cartilage of the transgenic mouse embryos, using TRIzol (Invitrogen, Carlsbad, CA), and was then reverse-transcribed for cDNA synthesis. Expression of the transgene was analyzed quantitatively by real-time quantitative PCR (MX3000P; Stratagene, La Jolla, CA). Primers were designed against the specific poly(A) region of the transgene, which is common to all 3 transgenes, namely 5′-GCGTGCATGCGACGTCATAGCTCTC-3′ (forward) and 5′-GGTTCAGGGGGAGGTGTGGGAGG-3′ (reverse). Four mice per group were analyzed.

Skeletal preparations. To prepare skeletal specimens for analysis, groups of mouse skeletons were dissected at each indicated time point of development and skinned. Subsequently, the skeletons were fixed in 100% ethanol at 4°C overnight, and stained with Alcian blue dye for 1 day followed by staining with alizarin red solution according to the standard protocol (7). Specimens were cleared in 50% glycerol/50% ethanol until soft tissue staining was removed. Six mice per group were analyzed, and identical phenotypes were observed.

Histology, in situ hybridization, and immunohistochemistry. For histologic examination, tissue samples from the embryos were immediately fixed in 4% paraformaldehyde/phosphate buffered saline after dissection, dehydrated with gradually increasing concentrations of ethanol, and embedded